



HAL
open science

Deciphering the conditions of tochilinite and cronstedtite formation in CM chondrites from low temperature hydrothermal experiments

Lionel Vacher, Laurent Truche, François Faure, Laurent Tissandier, Régine Mosser-ruck, Yves Marrocchi

► **To cite this version:**

Lionel Vacher, Laurent Truche, François Faure, Laurent Tissandier, Régine Mosser-ruck, et al.. Deciphering the conditions of tochilinite and cronstedtite formation in CM chondrites from low temperature hydrothermal experiments. *Meteoritics and Planetary Science*, 2019, 54 (8), pp.1870-1889. 10.1111/maps.13317 . hal-02357510

HAL Id: hal-02357510

<https://hal.univ-lorraine.fr/hal-02357510v1>

Submitted on 10 Nov 2019

HAL is a multi-disciplinary open access archive for the deposit and dissemination of scientific research documents, whether they are published or not. The documents may come from teaching and research institutions in France or abroad, or from public or private research centers.

L'archive ouverte pluridisciplinaire **HAL**, est destinée au dépôt et à la diffusion de documents scientifiques de niveau recherche, publiés ou non, émanant des établissements d'enseignement et de recherche français ou étrangers, des laboratoires publics ou privés.

17 **Abstract**—Tochilinite/cronstedtite intergrowths are commonly observed as alteration
18 products in CM chondrite matrices but the conditions under which they formed are still
19 largely under-constrained due to their scarcity in terrestrial environments. Here we report low
20 temperature (80°C) anoxic hydrothermal experiments using starting assemblages similar to
21 the constituents of the matrices of the most pristine CM chondrite and S-rich and S-free
22 fluids. Cronstedtite crystals formed only in S-free experiments under circumneutral conditions
23 with the highest Fe/Si ratios. Fe-rich tochilinite with chemical and structural characteristics
24 similar to chondritic tochilinite was observed in S-bearing experiments. We observed a
25 positive correlation between the Mg content in the hydroxide layer of synthetic tochilinite and
26 temperature, suggesting that the composition of tochilinite is a proxy for the alteration
27 temperature in CM chondrites. Using this relation, we estimate the mean precipitation
28 temperatures of tochilinite to be 120-160°C for CM chondrites. Given the different
29 temperature ranges of tochilinite and cronstedtite in our experiments, we propose that Fe-rich
30 tochilinite crystals resulted from the alteration of metal beads under S-bearing alkaline
31 conditions at $T = 120\text{-}160^\circ\text{C}$ followed by cronstedtite crystals in formed by reaction of matrix
32 amorphous silicates, metal beads, and water at low temperature (50–120°C).

33

INTRODUCTION

C-type asteroids are the sources of undifferentiated carbonaceous meteorites and provide valuable information about the physicochemical conditions that prevailed in the solar protoplanetary disk. CM carbonaceous chondrites are fragments of these asteroids (Clark et al. 2010; Cloutis et al. 2011) and contain a significant amount of water (i.e., water/rock ratio = 0.4 upon accretion; Marrocchi et al. 2018), mainly as OH bound into phyllosilicates (Jarosewich 1990; Barber 1981). They are characterized by different degree of aqueous alteration, from moderately (CM2) to highly altered (CM1) (Zolensky et al. 1997; Rubin et al. 2007), and contain a variety of secondary phases produced through aqueous alteration processes, including carbonates, sulfides, oxides, and hydroxides (Bunch and Chang, 1980; Barber 1981; Tomeoka and Buseck, 1985; Zolensky et al. 1993; Brearley, 2006; Howard et al. 2009, 2011; Lee et al. 2014). The most characteristic secondary phases in CM chondrites are tochilinite-cronstedtite intergrowths (TCIs), occurring as complex assemblages dispersed throughout the chondrules, fine-grained rims and matrix (Fuchs et al. 1973; Tomeoka and Buseck 1985; Nakamura and Nakamuta 1996; Howard et al. 2015; Pignatelli et al. 2016, 2017). TCIs are ubiquitous in unheated CM chondrites and may be useful in deciphering the alteration conditions of CM parent bodies.

Since the first description of complex Fe-S-O alteration minerals in CM chondrites (i.e., as “poorly characterized phases”; Ramdohr 1963; Fuchs et al. 1973), numerous studies have sought to better understand the mineralogy and chemical properties of TCIs (Tomeoka and Buseck 1985; Mackinnon and Zolensky 1984; Zolensky and Mackinnon 1986; Nakamura and Nakamuta 1996; Palmer and Lauretta 2011; Pignatelli et al. 2016, 2017). Two types of TCIs have been defined based on morphology, mineralogy, and chemical composition (Nakamura and Nakamuta 1996): Type-I TCIs occur as rounded massive rims around Fe-Ni metal beads embedded in chondrules and comprise tochilinite with minor cronstedtite and goethite (Palmer and Lauretta 2011; Pignatelli et al. 2017), whereas Type-II TCIs occur as fibrous clusters in the matrix and comprise cronstedtite with minor tochilinite and magnetite (Pignatelli et al. 2017).

Tochilinite is a hydroxysulfide mineral with the general ideal formula of $2\text{Fe}_{1-x}\text{S} \cdot n(\text{Fe},\text{Mg},\text{Al},\text{Ca})(\text{OH})_2$, where $0.08 \leq x \leq 0.28$ and $1.58 \leq n \leq 1.75$ (Zolensky and Mackinnon 1986; Gubaidulina et al. 2007). Its crystal structure is characterized by alternating brucite/amakinite-like $(\text{Mg},\text{Fe})(\text{OH})_2$ and mackinawite-like $(\text{Fe},\text{Ni})_{1-x}\text{S}$ layers (Mackinnon and Zolensky 1984; Organova et al. 1988). Meteoritic tochilinite is believed to form during

68 the first stage of aqueous alteration by dissolution of Fe-Ni metal or olivine/pyroxene by S-
69 and Fe-rich fluids (Zolensky and Mackinnon 1986; Palmer and Lauretta 2011; Pignatelli et al.
70 2016). Thermodynamic simulations and hydrothermal experiments indicate that tochilinite
71 precipitates under very reducing conditions ($\log f\text{O}_2 \approx -91$ to -85) in neutral-alkaline
72 environments ($\text{pH} = 7.8\text{--}14$), typically at $80\text{--}320^\circ\text{C}$ (Kakos et al. 1994; Browning and
73 Bourcier 1996; Kozerenko et al. 1996; Moroz et al. 1997; Gubaidulina et al. 2007; Peng et al.
74 2007; Peng and Jing 2014). Cronstedtite is a Fe-rich phyllosilicate (7 \AA along its c -axis) with
75 the general formula $(\text{Fe}^{2+}_{3-x}\text{Fe}^{3+}_x)(\text{Si}_{2-x}\text{Fe}^{3+}_x)\text{O}_5(\text{OH})_4$, where $0 \leq x \leq 0.84$ (Hybler et al. 2000;
76 Kogure et al. 2002; Pignatelli et al. 2013): Fe^{3+} is in tetrahedral coordination, and cronstedtite
77 forms a solid solution with greenalite $[(\text{Fe}^{2+}\text{Fe}^{3+})_3\text{Si}_2\text{O}_5(\text{OH})_4]$ and chrysotile
78 $[\text{Mg}_3\text{Si}_2\text{O}_5(\text{OH})_4]$ in CM chondrites (Velbel 2014). Some Type-II TCIs display euhedral
79 crystal faces suggesting that such TCIs result from the pseudomorphism of olivine, pyroxene,
80 and carbonates (Browning and Bourcier 1996; Lee et al. 2013; Pignatelli et al. 2016; Vacher
81 et al. 2017). Laboratory experiments and thermodynamic calculations suggest that cronstedtite
82 forms under less reducing conditions than tochilinite (i.e., $\log f\text{O}_2 \approx -75$ to -55) in neutral
83 conditions ($\text{pH} = 7\text{--}8$) from Si- and Fe-rich fluids at $50\text{--}120^\circ\text{C}$ (Lantenois et al. 2005; Lanson
84 et al. 2012; Pignatelli et al. 2013, 2014; Zolotov 2014).

85 The occurrence of tochilinite and cronstedtite as intergrowths suggests that (i) these
86 minerals may precipitated under similar physicochemical conditions at some point (Pignatelli
87 et al. 2016, 2017) and/ or (ii) one could have replaced the other during the CM parent body
88 evolution. Their stability fields remain poorly constrained, and few laboratory experiments
89 have investigated the formation of tochilinite and cronstedtite from starting products similar
90 to those encountered in CM chondrites (Peng et al. 2007; Peng and Jing 2014). To fill this
91 gap, we performed short-term (up to two months) anoxic hydrothermal experiments at 80°C
92 by reacting synthetic glass powder of a composition similar to the primitive chondrite matrix,
93 metal iron, and olivine with S-rich and S-free fluids. Specific attention was paid to the
94 mineralogical and chemical characterization of the reaction products and the implications for
95 the alteration conditions of CM chondrites.

96

MATERIAL AND METHODS

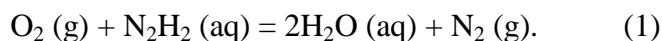
“Synthetic GEMS-like” glass preparation

Pristine CM chondrite matrix is mainly composed of amorphous silicate grains a few hundred nanometers in size that share many similarities with GEMS grains (glass with embedded metal and sulfides) observed in chondritic interplanetary dust particles (IDPs) (Bradley 1994; Keller and Messenger 2011; Leroux et al. 2015). We thus used an analogous starting material for our hydrothermal experiments. Synthetic glass (hereafter “synthetic GEMS-like glass”) containing 51.82 wt.% SiO₂, 25.80 wt.% MgO, 14.63 wt.% Fe₂O₃, 5.59 wt.% Al₂O₃, and 1.88 wt.% CaO (bulk analysis from SARM, Nancy, France), similar to natural GEMS grains (Leroux et al. 2015), was prepared from oxide carbonate powders (SiO₂, MgCO₃, Fe₂O₃, Al₂O₃, and CaCO₃) at CRPG (Nancy, France). The powder mixture was melted in platinum crucibles at 1550°C for 30 min and quenched in cold water. This quenched glass was crushed to a fine powder (particles of a few microns to a few hundred microns) in an agate mortar and pestle.

GEMS grains in IDPs contain rounded Fe-Ni metal grains believed to have formed in the hot inner regions of the solar protoplanetary disc by heating of amorphous silicate grains in a reduced environment at moderate temperatures (<730 °C, Davoisne et al. 2006). We therefore reduced our glass using the sealed evacuated silica glass method (Skykker and Luce 1971): the synthetic glass powder was loaded into graphite crucibles placed in sealed evacuated silica glass tubes (2×10^{-2} mbar) and heated at 1000°C for three days (**Fig. 1a**). After this reduction stage, a small amount of small beads of metallic iron (i.e., <1 vol.%), with sizes of a few microns to a few tens of microns, was observed in our synthetic glass (**Fig. 1b, c**).

Hydrothermal experiments

Hydrothermal experiments were performed by placing sample mixtures in Teflon® bowls within Parr® non-stirred pressure vessels. To remove oxygen trapped in the porosity of the Teflon® bowls, the bowls were pre-treated with a hydrazine solution (20 ppm N₂H₂) at 200 °C for one day. Oxygen gas was removed from the vessels according to the reaction (Dargent et al. 2015):



130 The reactors were then cleaned in a glove box under inert argon atmosphere (<1 ppm O₂)
131 using 1 M HCl and rinsed several times with MilliQ water. The solid starting products (i.e., 1
132 g comprising (i) synthetic GEMS-like glass, (ii) San-Carlos olivine [Mg_{1.8}Fe_{0.19}Ni_{0.01}SiO₄]
133 grains typically in the size range 20–50 μm, and (iii) spherical iron metal blobs <10 μm in
134 diameter from Sigma Aldrich) were mixed in various proportions (see **Table 1 and Fig. 2a**)
135 under inert Ar atmosphere in the glove box. The sample mixtures were then loaded together
136 with 10 mL of a synthetic saline solution (2.1 mM NaCl, 0.4 mM MgCl₂ and CaCl₂, pH = 6.5
137 at 25°C, **Table 1**) into the Teflon® Parr® bombs (**Fig. 2b**).

138 Previous laboratory experiments demonstrated that tochilinite and cronstedtite
139 preferentially precipitate under alkaline S-rich (the best tochilinite specimens at pH ≈ 11;
140 Kozerenko et al. 2001) and neutral S-free environments (pH ≈ 7; Pignatelli et al. 2013),
141 respectively. Hence, we separated our experiments into two sets: the first with an alkaline
142 environment created by adding 10 mM Na₂S to the initial saline solution (pH = 11.5 at 25°C)
143 and the second with a circumneutral environment employing only the initial salty solution
144 (pH = 6.5 at 25°C, **Table 1, Fig. 2b**). The water/rock ratio was set to 10 (by weight) and the
145 vessels were heated at 80°C and at saturated vapor pressure in a furnace for 30 or 60 days.
146 The two sets of experiments are summarized in **Table 1** and in **Figure 2**.

147 At the end of the experiments, the vessels were removed from the furnace and quenched
148 in cold water. The vessels were opened and the solid products were dried in a glove box under
149 argon atmosphere at room temperature.

150

151 **Solution analysis**

152

153 The run solutions were immediately extracted from the vessels after quenching, filtered at
154 0.02 μm, and separated into two distinct aliquots for (i) pH measurement at room temperature,
155 and (ii) inductively coupled plasma optical emission spectrometry (ICP-OES) analyses. ICP-
156 OES analyses were performed after dilution in HNO₃ (2 vol.%) to determine the
157 concentration of dissolved Al, Ca, Fe, K, Mg, Na, and Si (detection limit < 50 μg/L). Because
158 dissolved Al, Fe, and Mg were below the detection limit in run solutions G-2, GO-2, and
159 GOI-2, additional aliquots (without dilution) were collected and measured by inductively
160 coupled plasma mass spectrometry (ICP-MS) at SARM (Nancy, France) with a detection
161 limit < 1 μg/L.

162

163 **Characterization techniques**

164

165 Back-scattered electron (BSE) images of the solid products were obtained at
166 GeoRessources (Nancy, France) using a JEOL J7600F Field Emission Scanning Electron
167 Microscope (FE-SEM) equipped with an Oxford EDS (Energy Dispersive X-ray
168 spectrometer). SEM observations were performed with an accelerating voltage of 15 kV. EDS
169 analyses were made with an accelerating voltage of 15 kV and a beam current of 100nA.
170 Chemical analyses were calibrated using the following natural minerals: albite for Al,
171 hematite for Fe and O, olivine for Mg, orthoclase for Si, wollastonite for Ca and FeS₂ for S.

172 Solid products were prepared for transmission electron microscopy (TEM) and scanning
173 transmission electron microscopy (STEM) by crushing them in an agate mortar, dispersing
174 them in an ethanol solution under ultrasonic treatment, and evaporating the solution on a
175 holey carbon film placed on a 200 mesh copper grid. TEM imaging, EDX analyses and
176 selected area electron diffraction (SAED) were performed at IJL (Nancy, France) using a
177 JEM-ARM 200F cold-field emission gun TEM/STEM operating at 200 kV and equipped with
178 a spherical aberration (Cs) probe corrector (0.19 and 0.078 nm point resolution in TEM and
179 STEM mode, respectively). Qualitative measurement of elements was obtained using the
180 Cliff-Lorimer ratio method. Electron-transparent cross-sections of samples from GS-2 and
181 GOS-2 were prepared by using a FEI Versa 3D DualBeam field emission (FIB/SEM) at the
182 F.M.E company (Nancy, France).

183 The hydrated/porous nature and the small sizes (less than 1 μm) of the secondary mineral
184 phases synthesised during our hydrothermal experiments make the SEM-EDS analyses
185 difficult. However, we excluded all the analyses with a total lower than 65 wt.% (lowest total
186 measured in the Fe, Si-rich layer in the S-bearing experiments) and higher than 102 wt.%. In
187 addition, all the representative chemical compositions reported in the Tables S1 and S3 were
188 normalized to 100%.

189 X-ray diffraction (XRD) data were collected at room temperature with a PANalytical
190 X'pert PRO diffractometer (goniometer θ -2 θ), using a Cu tube, a Ge (111) incident-beam
191 monochromator ($\lambda = 1.5406 \text{ \AA}$) and a X'Celerator detector (scanning line detector 1D, 2.122°
192 active length) at CRM laboratory (University of Lorraine, France). X-ray patterns were
193 collected on bulk-rock samples, with 2.122° active length, using a scan step of 0.0167° (2 θ)
194 and a time of measurement for each sample of 90min, $2\theta_{\text{min}} = 5^\circ$ to $2\theta_{\text{max}} = 70^\circ$.

195

196

197 35 kV accelerating voltage and 45 mA current (CRM laboratory, University of Lorraine,
198 France). X-ray patterns were collected on bulk-rock samples, using a scan step of 0.007° (2θ)
199 and a time of measurement for each sample of 90min, $2\theta_{\min} = 5^\circ$ to $2\theta_{\max} = 70^\circ$.

RESULTS

Circumneutral S-free experiments

Solid phase characterization

Alteration of primary phases

SEM observations of olivine and synthetic GEMS-like grains do not reveal obvious signs of dissolution on grain surfaces or along grain boundaries (e.g., disk-shaped grains or the formation of a gel layer) at micrometer scale (**Fig. S1**). However, this lack of evidence does not exclude minor signs of dissolution at nanometer scale, but further FIB–TEM investigations are required. In contrast, corrosion textures characterized by thin layers of newly formed material are present at the edges of iron metal grains (**Fig. 3b**).

Secondary mineral paragenesis

SEM-TEM observations of the S-free run products reveal the presence of two new mineral phases synthesized during the hydrothermal experiments. The first is present in the run products of all three S-free experiments and is composed of a fibrous Fe-Si-rich mineral occurring in layers <1 μm thick around native iron metal (**Fig. 3b**). This phase has a composition close to berthierine or greenalite ($n = 2$, **Fig. 3c, Table S1**).

The second new phase is an iron oxide that occurs only in experiment GOI as grains of a few tens of microns (**Fig. 3a**). This phase is easily identifiable at contacts with iron metal grains. SEM-EDS analyses indicate that this iron oxide has a composition close to goethite: 65.4 ± 2 wt.% Fe, 31.1 ± 1.5 wt.% O, 3.2 ± 0.5 wt.% Si, 0.1 ± 0.3 wt.% Mg, and 0.03 ± 0.1 wt.% Ca ($n = 11$, 1σ errors; **Fig. 3c, Table S1**).

Cronstedtite precipitation

Detailed TEM investigation of experiment GOI reveals rare triangular crystals of cronstedtite <1 μm in size that were not detected by X-ray diffraction (XRD) (**Fig. 4a, b**). Cronstedtite was not detected in the products of experiments G and GO. TEM-EDS measurements show that these crystals contain of 52.8 ± 1.9 wt.% Fe, 36.9 ± 1.7 wt.% O, 8.3 ± 0.4 wt.% Si, 1.4 ± 0.2 wt.% Al, 0.4 ± 0.1 wt.% Mg, and 0.2 ± 0.1 wt.% Ca ($n = 6$, 1σ errors; **Fig. 4a, Table S1**). To calculate the average structural formula of cronstedtite, the $\text{Fe}^{3+}/\text{Fe}^{2+}$ ratio was adjusted to set the occupancy of the octahedral sites to 3 following

233 Pignatelli et al. (2013). Hence, based on a total of 7 oxygen atoms, we obtained the mean
234 empirical formula of cronstedtite to be $(\text{Fe}^{2+}_2\text{Fe}^{3+}_{0.9}\text{Mg}_{0.1})(\text{Si}_{1.1}\text{Al}_{0.2}\text{Fe}^{3+}_{0.7})\text{O}_5(\text{OH})_4$. The
235 SAED pattern along the [001] zone axis of cronstedtite (**Fig. 4d**) reveals: (i) strong $h - k = 3n$
236 diffractions (e.g., 110, 300, in hexagonal indexing) and weak $h - k \neq 3n$ diffractions (e.g.,
237 100, 010, 200), and (ii) a hexagonal cell with parameters $a = b = 0.54$ nm (**Fig. 4c, d**). The
238 SAED pattern along the [010] zone axis indicates the cell parameter $c = 0.71$ nm (**Fig. 4e, f**),
239 consistent with typical terrestrial (Hybler et al. 2000) and meteoritic cronstedtite (i.e.,
240 polytype 17; Pignatelli et al. 2018).

241

242 *Solution chemistry*

243 The evolution of Si, Ca, Mg, and Fe concentrations in the neutral S-free experiments are
244 presented in **Fig. 5a–c** and **Table S2**. After two months, Si concentrations reached a steady
245 state (within errors) at 0.8 and 0.4 mM in experiments G and GOI, respectively (**Fig. 5a, c**). In
246 experiment GO, the Si concentration increased to 1.2 mM after one month, then decreased to
247 0.6 mM after two months (**Fig. 5b**). Calcium concentrations remained rather constant at ~0.3
248 mM in experiments G and GO and at ~0.25 mM in experiment GOI (**Fig. 5a–c**). Magnesium
249 concentrations decreased from 0.4 to ~0.05 mM over two months in all S-free experiments
250 (**Fig. 5a–c**). Iron and Al concentrations remained very low, $\sim 10^{-4}$ to 10^{-3} mM, after two
251 months in all the experiments (**Fig. 5a–c, Table S2**). The elevated Fe concentrations (from 23
252 to 78 mM) after one month are surprising and may reflect a strong
253 solution disequilibrium with respect to Fe-bearing minerals (e.g. magnetite, greenalite and
254 cronstedtite) expected to be stable under our experimental. Indeed, thermodynamic
255 simulations performed with PhreeqC software together with the Ilnl database indicate
256 that dissolved iron concentration should remain within the 10^{-4} to 10^{-6} mM range under our
257 experimental conditions (i.e., $T = 80^\circ\text{C}$, $\text{pH} = 6\text{--}8$ and $\log f\text{O}_2 = -60$) if the fluid is in
258 equilibrium with magnetite, greenalite or cronstedtite. Thus, the elevated Fe concentrations
259 observed in our run solutions either result from (i) a precipitation delay of Fe-bearing
260 minerals (causing an oversaturation of Fe) or (ii) a contamination/filtration issue. In the
261 absence of a continuous monitoring of solution composition over time, it is difficult to
262 provide a robust explanation for this observation.

263 The pH of the solutions increased progressively up to pH = 8 in experiments GO and GOI,
264 but decreased slightly to pH = 6 in experiment G (**Fig. 5d; Table S2**).

265

266 **Alkaline, S-rich experiments**

267

268 *Solid Phase characterization*

269 *Alteration of primary phases*

270 SEM observations of the primary phases after reaction do not reveal obvious signs of
271 dissolution on olivine and synthetic GEMS-like grains at the micrometer scale (**Fig. S1**). In
272 contrast, a thin (1–2 μm) iron oxide layer penetrates the surfaces of iron metal grains.

273

274 *Secondary mineral paragenesis*

275 SEM observations of products of the S-bearing experiments show newly formed synthetic
276 assemblages 2–3 μm thick around iron metal beads (not detected by XRD analysis) (**Fig. 6a,**
277 **b**). This mineral assemblage can be separated into three different layers according to the
278 textures observed: (i) a compact layer penetrates the metal grains and exhibits irregular
279 contacts with the iron metal, (ii) a secondary rim with an acicular/fibrous texture surrounds
280 the compact layer, and (iii) a fibrous layer surrounds the acicular layer (**Fig. 6a, b**).

281 The TEM chemical profile of the alteration rims in the GS-2 FIB-produced cross section
282 (**Fig. 7a, e**) shows chemical zoning of Fe, O, S, and Si within the different layers (**Fig. 7b–e**).
283 The inner compact zone (Z_1) is Fe- and O-rich (**Fig. 7c**) and is characterized by homogeneous
284 Fe, O, Si, and S concentrations averaging 61.6, 29.8, 4.8, and 3.7 wt.%, respectively ($n = 3$,
285 **Fig. 5c**). The acicular/fibrous layer (Z_2) is Fe- and S-rich is compositionally zoned: Fe and S
286 concentrations are highest in the center of the layer (67.5 and 23.2 wt.%, respectively) and
287 decrease towards the surrounding layers (down to ~62 and 9.5 wt.%, respectively), whereas O
288 and Si concentrations are lowest in the center of the layer (8.4 and 0.9 wt.%, respectively) and
289 increase towards the surrounding layers (reaching 24.5 and 4 wt.%, respectively) ($n = 5$, **Fig.**
290 **7e**). The outer zone (Z_3) is also Fe- and O-rich, but contains higher O and Si concentrations
291 (39.4 and 10.6 wt.%, respectively) and lower Fe and S concentrations (49.3 and 0.7 wt.%,
292 respectively) than layers Z_1 and Z_2 (**Fig. 7e**). A layer similar to Z_3 occurs between layers Z_1
293 and Z_2 with variable thickness (**Fig. 7a–d**).

294

295 *Tochilinite precipitation*

296 TEM imaging of the acicular Fe-S-rich layer (Z_2) indicate that this assemblage comprises
297 many needle-shaped crystals several hundreds of nanometers in size (**Fig. 8a, b**). High-
298 resolution TEM (HRTEM) images suggest that these crystals grew perpendicular to the

299 surface of the iron metal grain (**Fig. 8b–c**). However, the corresponding SAED pattern
300 (collected from a small area of the needle-shaped crystals) indicates that this assemblage is
301 poorly crystalline and shows several strong and weak broad rings at *d*-spacings of 0.54, 0.27,
302 0.25 and 0.18 nm, compatible with tochilinite reflections (**Fig. 8d**; Organova et al. 1973;
303 Pekov et al. 2013). Furthermore, HRTEM images indicate lattice fringes of 0.54 nm and
304 SAED patterns show strong (002) diffraction spots along the *c** axis consistent with
305 tochilinite (**Fig. 8e, f**) (Mackinnon and Zolensky 1984; Organova et al. 1988; Kakos et al.
306 1994). EDX analyses of isolated acicular crystals show that they contain variable
307 concentrations of Fe and O, with the average composition 57.9 ± 9.4 wt.% Fe, 18.4 ± 5.7
308 wt.% O, 17.9 ± 1.5 wt.% S, 3.9 ± 2 wt.% Si, 0.7 ± 0.8 wt.% Ca, and 0.6 ± 0.8 wt.% Mg (*n* =
309 6, 1σ errors; **Fig. 6c, Table S3**). These analyses demonstrate that the acicular crystals
310 forming the intermediate rims around iron grains are tochilinite with a mean empirical
311 formula equivalent to $2(\text{Fe}_{0.88}\text{S}) \cdot 2.1(\text{Fe}_{0.96}\text{Mg}_{0.04})(\text{OH})_2$ when normalized to 2 S atoms.

312

313 *Solution chemistry*

314 Si and Ca concentrations of the experimental solutions are plotted as a function of elapsed
315 time in **Fig. 9a–c** and **Table S2**. Si concentrations in the solution increased over two months
316 to reach a steady state (within error) at 1.7 and 1.9 mM in experiments GS and GOS,
317 respectively (**Fig. 9a, b**). In experiment GOIS, the Si concentration increased to 1.1 mM after
318 one month, then decreased to 0.3 mM after two months (**Fig. 9c**). Ca concentrations decreased
319 from 0.4 mM to 0.01–0.02 mM after two months in all the S-bearing experiments (**Fig. 9a–c**).
320 Fe, Mg, and Al concentrations are very low, with most measurements below the ICP-OES
321 detection limit (i.e., <50 µg/L, **Table S2**).

322 The pH of the S-rich alkaline solutions decreased from 11.5 to 7.7 and 8.8 over two
323 months in experiments GS and GOS, respectively (**Fig. 9d**). In experiment GOIS, the pH
324 decreased to 6.4 after one month, then increased to 9.7 after another month (**Fig. 9d**).

325

DISCUSSION

326
327
328
329
330
331
332
333
334
335
336
337

These low temperature hydrothermal experiments aimed to investigate the formation of meteoritic tochilinite and cronstedtite from starting products similar to the constituents of the matrices of the most pristine CM chondrite. We first explore the conditions of formation of tochilinite and cronstedtite by comparing our results to previous works on TCIs in CM chondrites and from laboratory experiments. We then estimate the temperatures of formation of CM tochilinite based on their Mg concentration and discuss the implications of these temperatures on understanding the thermal evolution of the CM parent body. We finally conclude the discussion by considering the possibility that tochilinite and cronstedtite may co-precipitate under similar physicochemical conditions for at least a short time.

Conditions of cronstedtite formation

338
339
340
341
342
343
344
345
346
347
348
349
350
351
352
353
354

Cronstedtite crystals formed only in the experiment with the highest Fe content (with GEMS-like grains, forsterite, and Fe^0 in equal proportions by mass; $\text{Fe}_{\text{tot}}/\text{Si} = 2.7$). This result is in good agreement with the preferential formation of 1:1 (TO) iron phyllosilicates (i.e., cronstedtite/greenalite) reported for experiments with Fe/Si ratios of 2.25, whereas experiments with lower Fe/Si (i.e., 0.75) produced 2:1 (TOT) iron phyllosilicates (Mizutani et al. 1991). It thus appears that the Fe/Si ratio could be a key parameter controlling the formation of cronstedtite, with the presence of Fe^0 imposing reducing condition (H_2 is a by-product of Fe^0 oxidation under anoxic conditions) and providing Fe^{2+} for cronstedtite precipitation. In addition, experiments and thermodynamic modeling have shown that cronstedtite crystals form under specific conditions: $\text{pH} = 7\text{--}8$, $\log f\text{O}_2 \approx -65$ to -60 (estimated from the measured Si concentrations in solutions from experiment GOI and the calculated stability field of cronstedtite at 80°C from Pignatelli et al. 2014, **Fig. 10**), and below 100°C because the stability field of cronstedtite decreases with increasing temperature (**Fig. 10**; Rivard 2001; Schulte and Shock 2004; McAlister and Kettler 2008; Zolotov 2014; Pignatelli et al. 2013, 2014).

355
356
357
358

Our results indicate that the cronstedtite formed by reaction between synthetic GEMS-like glass, metallic iron, and water. Similarly, in the least altered CM chondrite Paris (Hewins et al. 2014, Marrocchi et al., 2014), (i) the occurrence of platy cronstedtite in association with amorphous silicates and serpentines and (ii) the progressive iron enrichment of the matrix

359 resulting from the dissolution of Fe-Ni metal beads (Leroux et al. 2015) suggest that
360 cronstedtite formed from fluid reaction with matrix amorphous silicates, Fe-Ni metal beads,
361 and water (melted accreted ices) in CM chondrites.

362 In CM chondrites, cronstedtite-like crystals probably correspond to a ternary solid
363 solution and/or mixture between greenalite $((\text{Fe}^{2+}\text{Fe}^{3+}\text{Mg}\square)_3(\text{SiAl})_2\text{O}_5(\text{OH})_4$; Guggenheim et
364 al. 1982), chrysotile $(\text{Mg}_3\text{Si}_2\text{O}_5(\text{OH})_4$) and cronstedtite end members (Velbel 2014, Pignatelli
365 et al. 2015). However, pure cronstedtite (i.e., cronstedtite with crystallo-chemical
366 characteristics similar to those reported for terrestrial one) has recently been identified and
367 characterized in CM Paris (Pignatelli et al. 2017, 2018). The chemical composition of our
368 synthetic cronstedtite is in good agreement with both terrestrial and pure cronstedtite in CM
369 Paris (Hybler et al. 2000; Pignatelli et al. 2018) (see **Fig. 3c**). Thus, cronstedtite in CM Paris
370 probably formed under similar conditions to those investigated herein: i.e., high Fe/Si ratio
371 (resulting from the progressive incorporation of Fe into the matrix by dissolution of iron
372 metal/kamacite and Fe-sulfide grains and precipitation of Fe-rich phyllosilicate, Leroux et al.
373 2015), $\sim 80^\circ\text{C}$, and in a circumneutral environment ($\text{pH} = 7\text{--}8$).

374

375 *Experimental and natural conditions of tochilinite formation*

376

377 *Condition of tochilinite formation*

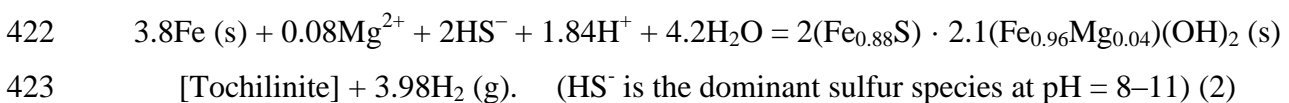
378 Few studies have succeeded in synthesizing (Fe,Mg)-tochilinite with Fe and Mg
379 concentrations similar to those in meteoritic tochilinite (see overview in **Tables 2** and **S4**;
380 Kozerenko et al. 1996, 2001; Chistyakova et al. 2006). In CM chondrites, tochilinite is Fe-
381 rich (40–58 wt.% Fe) and the Mg content of its brucite/amakinite-like layer is low (1–5 wt.%
382 Mg, **Table S4**; Palmer and Lauretta 2011; Pignatelli et al. 2017). Kozerenko et al. (1996)
383 produced Fe-rich tochilinite in low temperature (80°C) hydrothermal experiments by
384 depletion of Mg in solution. Chistyakova et al. (2006) and Gubaidulina et al. (2007)
385 synthesized Fe-rich tochilinite crystals in multiple series of experiments at $160\text{--}180^\circ\text{C}$ with
386 various Mg contents in the initial mixture (0.67–4.17 mmol; Gubaidulina et al. 2007), but
387 yielded minor Mg contents in the brucite layer ($n\text{Mg} = 0.02\text{--}0.36$, where $n\text{Mg}$ is Mg content
388 in the brucite layer normalized to 1 S). However, in these laboratory studies, iron was directly
389 supplied in solution as dissolved Fe^{2+} (FeCl_2 solution) and not by dissolution of Fe-Ni metal
390 beads as is the case in primitive chondritic material. Furthermore, these studies do not provide
391 the source of Mg in their starting products (Kozorenko et al. 2001; Chistyakova et al. 2006;

392 Gubaidulina et al. 2007).

393 We produced tochilinite from the alteration of synthetic glass and metallic iron, valuable
394 analogues of the amorphous silicates and Fe-Ni metal beads found in CM chondrite matrices
395 (Leroux et al. 2015). Dissolution of our synthetic glass is confirmed by the presence of
396 dissolved Si in all run solutions, especially experiments using only GEMS-like glass as the
397 starting material (**Table S2**), and the presence of Al in all S-free run solutions. We also noted
398 that Si concentrations are higher in S-bearing than S-free experiments, whereas the opposite is
399 observed for Mg (see **Table S2**). The difference in Si concentration is probably related to the
400 different pH values of the initial solutions, as glass dissolution increases with increasing pH in
401 neutral-alkaline conditions (Declercq et al. 2013; Vienna et al. 2018), whereas the dissolved
402 Mg concentration is controlled by the precipitation of secondary Mg-bearing minerals such as
403 brucite (not detected) and/or tochilinite in S-bearing alkaline environments (Zolotov 2014).

404 Tochilinite synthesized in this study displays chemical and textural similarities to
405 meteoritic tochilinite, such as (i) low Mg content (0–1.9 wt.% or 0.5 ± 0.7 wt.% Mg, 1σ , $n =$
406 6, **Table S4**), (ii) acicular morphology (**Fig. 8b**, Lee and Ellen 2008; Haack et al. 2012), and
407 (iii) preferential occurrence around iron metal grains (**Figs. 6a, b and 7a**; Palmer and Lauretta
408 2011). To our knowledge, this is the first time that tochilinite has been synthesized with
409 characteristics so close to those of meteoritic tochilinite and from experimental conditions
410 analogous to those of CM chondrite alteration. Peng and Jing (2014) also precipitated
411 tochilinite from synthetic (Fe-, Mg-, Si-, Al-, and Ni-rich) metal particles under high pH and
412 S concentrations (pH = 13–14, $[S^{2-}] = 10^{-2}$ to 10^{-1} mol/L) at 110–160°C, but their synthetic
413 mineral contained more Mg ($nMg = 0.46$, $1\sigma = 0.1$, $n = 4$) than CM tochilinite.

414 In CM chondrites, most tochilinite in Type-I TCIs formed during the earliest stages of
415 alteration from dissolution of kamacite by a S-rich fluid under alkaline conditions and
416 temperatures up to 130°C (Mackinnon and Zolensky 1984; Kozerenko et al. 2001; Palmer and
417 Lauretta 2011; Pignatelli et al. 2016, 2017). In our S-bearing experiments, Fe-rich tochilinite
418 systematically surrounds iron metal grains, regardless of the starting materials and the
419 proportion of metallic iron (**Fig. 6a, b**). Based on our SEM and TEM observations, we
420 propose that the formation of tochilinite is induced by dissolution-precipitation reactions
421 occurring at the metallic iron (or kamacite)-tochilinite interface as:



424 Due to the low solubility of secondary iron-bearing minerals, particularly tochilinite, the
425 reaction is Fe-conservative under our experimental conditions, as evidenced by the constant

426 and very low iron content of the reacting fluids. We also propose that the coupling between
427 iron dissolution and tochilinite precipitation is due to the interplay between substrate-
428 mediated nucleation and solution chemistry at the reaction front (**Figs. 6 and 7**). This is
429 texturally evident, as very small tochilinite crystallites grew inside the native-iron dissolution
430 pits and perpendicular to the reaction front. The proximity of the source and sink of iron
431 suggests that tochilinite nucleates easily and probably grows faster than the rate of iron
432 dissolution.

433 Tochilinite precipitation leads to a decrease in S concentration (i.e., consumption of all
434 the S initially in the fluid, **Fig. 9d, Table S2**). Once sulfide activity is no longer sufficient to
435 sustain tochilinite precipitation, Fe-Si-rich phyllosilicates are formed around tochilinite (e.g.,
436 greenalite and/or cronstedtite). Similarly, the outer parts of Type-I TCI rims in CM Paris are
437 mainly composed of Fe-silicates similar to cronstedtite (Pignatelli et al. 2016), though in our
438 experiments, the Fe-Si-rich fibrous phase bordering tochilinite (**Fig. 6a, b**) is more similar to
439 greenalite than cronstedtite (**Fig. 6c, Table S1**). These textural and chemical arguments
440 provide clear evidence for the fluid-mediated precipitation of tochilinite.

441

442 *Tochilinite: a proxy of the thermal history of CM chondrites?*

443 The synthetic tochilinite formed during our hydrothermal experiments was almost entirely
444 made up of amakinite layers (i.e., 96% Fe in the hydroxide layer), with minor Mg (4%). Other
445 tochilinite syntheses at 80–130°C show comparable Fe contents, with all Fe in the hydroxide
446 layer (Kozerenko et al. 1996, 2001), whereas those at a temperature of >130°C have 30–70%
447 Mg for $n = 1.5$ – 1.9 in the tochilinite formula (Kakos et al. 1994; Kozerenko et al. 2001;
448 Chistyakova et al. 2006; Gubaidulina et al. 2007; Peng and Jing 2014). It has been proposed
449 that Fe-tochilinite is metastable, with a kinetically controlled formation that requires depletion
450 of Mg^{2+} from solution and sufficiently high Fe^{2+} and S^{2-} activities at low temperature
451 (Kozerenko et al. 2001; Peng et al. 2007; Pekov et al. 2013). Nevertheless, Kozerenko et al.
452 (2001) demonstrated that the two main parameters controlling the stability field of tochilinite
453 are sulfide concentration and temperature. At S^{2-} concentrations between 1×10^{-3} and 5×10^{-5}
454 mol/L, Fe-tochilinite is stable up to 130°C, and (Mg,Fe)-tochilinite is the dominant phase at
455 130–320°C in the mackinawite-magnetite-pyrrhotite paragenesis (Kozerenko et al. 2001).
456 Other experiments above 130°C produced tochilinite with variable nMg contents, ranging
457 from 0.26 at 160–180°C to 0.66 at 200°C, but none with only amakinite layers (Kakos et al.
458 1994; Kozerenko et al. 2001; Chistyakova et al. 2006; Peng and Jing 2014).

459 In CM chondrites, tochilinite has low concentrations of Mg, ranging from 1.6 to 4.5 wt%
460 (Palmer and Lauretta 2011; Pignatelli et al. 2017). This difference in composition is also
461 correlated with degree of alteration of CM chondrites, which could reflect more availability of
462 Mg in solution from the dissolution of forsterite/pyroxene precursors (Hanowski and Brearley
463 2001). Nevertheless, no strong relationships have been established experimentally between
464 the Mg content in the starting products and that in tochilinite (Chistyakova et al. 2006). This
465 discrepancy is evident in the meteoritic tochilinite of CM Paris, which displays only minor
466 Mg in its structural formula (Mg = 1.6 wt%, **Table S4**) although it is thought to have formed
467 by the pseudomorphism of ferromagnesian silicate precursors (Pignatelli et al. 2016, 2017), so
468 there should have been abundant Mg available.

469 Thus, temperature could be the most important control on the Mg content in the
470 brucite/amakinite-like layer of tochilinite. Plotting the nMg content of the hydroxide layer of
471 synthetic tochilinite as a function of synthesis temperature reveals a positive trend defined by
472 $T = 175.9 (\pm 44.6) \times \text{nMg} + 100.4 (\pm 17.3)$ ($r^2 = 0.72$, $n = 8$) (**Fig. 11, Table S4**). Using this
473 correlation, meteoritic tochilinite with nMg contents of 0.12–0.32 (**Table S4**, Palmer and
474 Lauretta 2011; Pignatelli et al. 2017) correspond to mean precipitation temperatures of $122 \pm$
475 38°C for Paris ($n = 2$), $132 \pm 43^\circ\text{C}$ for Murchison ($n = 3$), $130 \pm 50^\circ\text{C}$ for Murray ($n = 3$), 157

476 $\pm 48^{\circ}\text{C}$ for Cold Bokkeveld ($n = 2$) and 153°C ($\pm 47^{\circ}\text{C}$) for Nogoya ($n = 1$). These
477 temperatures are higher than the predicted range of precipitation temperatures of (i) CM
478 carbonates estimated from bulk and *in situ* oxygen isotopic measurements and ‘clumped’
479 isotopes ($0\text{--}110^{\circ}\text{C}$; Clayton and Mayeda, 1984; Benedix et al. 2003; Guo and Eiler, 2007,
480 Verdier-Paoletti et al., 2017) and (ii) cronstedtite deduced from hydrothermal experiments
481 and thermodynamic data (i.e., $50 \leq T \leq 120^{\circ}\text{C}$; Pignatelli et al. 2013, 2014; Zolotov 2014).

482 These elevated average precipitation temperatures of meteoritic tochilinite indicate that
483 CM carbonates cannot be formed at the same time as meteoritic tochilinite. This result is
484 consistent with petrographic observations that indicate that primary carbonates (i.e., type 1a
485 calcite; Lee et al. 2014) precipitated at the earliest stages of alteration, before their partial or
486 complete replacement by TCIs (Lee et al. 2013; Vacher et al. 2017). Taking together, the
487 formation temperatures and the mineralization sequence of carbonate and tochilinite minerals
488 suggest an increase of the temperature during the duration of aqueous alteration, from $0\text{--}70^{\circ}\text{C}$
489 for carbonate to $120\text{--}160^{\circ}\text{C}$ for tochilinite (**Fig. 12**). Furthermore, the chemical zoning
490 observed in Type-II TCIs (i.e., the Fe- and S-enrichment at the border and the Fe- and Si-
491 enrichment toward the center; Pignatelli et al. 2016) indicates that cronstedtite may
492 precipitated after tochilinite, due to the decrease of the sulfur activity during the duration of
493 aqueous alteration (Pignatelli et al. 2017). If so, the range of low formation temperatures of
494 cronstedtite implies that this mineral may precipitated during the cooling phase of the CM
495 parent body, between 50 and 120°C (**Fig. 12**). This result is in good agreement with
496 experimental data that demonstrated that the development of crystals of cronstedtite is likely
497 promoted by a temperature decrease during the course of alteration (Pignatelli et al. 2013).

498 Therefore, the Mg content of tochilinite seems to be a powerful proxy in order estimate
499 the alteration temperature of CM chondrites. However, we note that this correlation is based
500 on a small amount of data and further hydrothermal experiments are needed to better
501 understand the role of the other physiochemical parameters (e.g., pH, W/R ratio, starting
502 assemblage or solution chemistry) in controlling of the Mg content of tochilinite.

503 *Co-precipitation of tochilinite and cronstedtite in CM chondrites?*

504 In CM chondrites, tochilinite has been proposed to precipitate during the first stages of
505 aqueous alteration under very low oxygen fugacity (Browning and Bourcier 1996), neutral-
506 alkaline pH (Kozerenko et al. 1996; Peng et al. 2007; Peng and Jing 2014), and at 80–320°C
507 (Kozerenko et al. 1996, 2001), whereas cronstedtite forms under less reduced conditions than
508 tochilinite due to the presence of Fe³⁺ (Pignatelli et al. 2014), in circumneutral pH
509 environments (Pignatelli et al. 2013), and below 120°C (Lantenois et al. 2005; Lanson et al.
510 2012; Pignatelli et al. 2013, 2014) (**Fig. 13**). Therefore, it has been proposed that CM
511 chondrite alteration conditions changed during alteration, with the initial precipitation of
512 tochilinite followed by the formation of cronstedtite (Pignatelli et al. 2016). However,
513 tochilinite is frequently observed in close association with cronstedtite in Type-II TCIs at both
514 the micron and the nanometer scales (Mackinnon and Zolensky 1984; Haack et al. 2012;
515 Leroux et al. 2015; Pignatelli et al. 2016, 2017). This complex intergrowth indicates that (i)
516 tochilinite and cronstedtite may co-precipitated under similar physicochemical conditions for
517 at least a short time (Palmer and Lauretta 2011; Pignatelli et al. 2016) and/or (ii) cronstedtite
518 could have replaced tochilinite during the course of alteration. Identifying which of these two
519 scenarios prevailed is not an easy task, because the intergrowth between tochilinite and
520 cronstedtite can be attributed to either of these two processes. Nevertheless, because
521 tochilinite and cronstedtite have been formed under similar physicochemical conditions in our
522 experiments (i.e., 80°C and pH ≈ 8), here we explore the possibility that they both could have
523 been formed at the same time.

524 We did not observe cronstedtite crystals in our S-bearing experiments, though we
525 expected cronstedtite to form in experiment GOIS due to (i) the similar proportion of starting
526 assemblages as the cronstedtite-producing S-free experiment GOI and (ii) the favorable
527 concentration of Si in the run solutions (**Table S2, Fig. 13**). This lack of cronstedtite
528 formation may have explained by the final alkalinity of the experiment (pH = 9.7) preventing
529 cronstedtite precipitation (Pignatelli et al. 2015) or the reaction time being too short under the
530 experimental conditions to produce abundant cronstedtite of a high degree of crystallinity
531 compared to longer syntheses (**Table 2**).

532 Nonetheless, the occurrence of tochilinite and cronstedtite at 80°C in the S-rich and S-free
533 experiments, respectively, suggests that both minerals might form at similar aqueous
534 alteration temperatures. Because the stability field of cronstedtite is expected to diminish with
535 increasing temperature (Pignatelli et al. 2014; Zolotov 2014) and cronstedtite was not

536 observed in experiments at $\geq 150^\circ\text{C}$ (Rivard 2011; Pierron 2011), co-precipitation of
537 tochilinite and cronstedtite implies a restrictive alteration temperature range of $80\text{--}120^\circ\text{C}$
538 (**Fig. 12**). Following the same logic, in our experiments, cronstedtite formed at $\text{pH} \approx 7\text{--}8$ and
539 tochilinite at $\text{pH} = \sim 8\text{--}11$, consistent with previous results for cronstedtite ($\text{pH} = 7.2\text{--}7.6$;
540 Pignatelli et al. 2013) and tochilinite ($\text{pH} = 7.3\text{--}11.4$; Kozorenko et al. 1996). Thus, co-
541 precipitation of tochilinite and cronstedtite should indicate a circumneutral environment of pH
542 $= 7\text{--}8$.

543 Quantitative estimation of the redox conditions of tochilinite and cronstedtite co-
544 precipitation is more problematic because, according to thermodynamic modelling, these two
545 minerals do not share a common $f\text{O}_2$ range (**Fig. 13**; Browning and Bourcier 1996; Dyl et al.
546 2006; Pignatelli et al. 2014). The $f\text{O}_2$ of cronstedtite precipitation is well constrained in our
547 experiments due to the limited variation of Si concentrations in the associated run solutions
548 (i.e., $\text{Si} \approx 4 \text{ mM}$, **Table S2**), implying $f\text{O}_2$ conditions in the range $\log f\text{O}_2 = -62$ to -58 at 80°C
549 (**Figs. 10 and 13**). However, we cannot directly estimate the $f\text{O}_2$ for our synthetic tochilinite
550 due to the limited available information on its stability. Browning and Bourcier (1996)
551 showed that the stability of Fe-rich tochilinite implies extremely reducing conditions
552 compared to cronstedtite, i.e., $\log f\text{O}_2 = -91$ to -85 , though this range of oxygen fugacity is
553 relevant at 0°C (Fujiya et al. 2015), too cold for the formation of meteoritic tochilinite. With
554 increasing temperature, the stability fields of Fe-O-S minerals move toward higher $f\text{O}_2$ and $f\text{S}_2$
555 (Holland 1959), as demonstrated in **Fig. 13**. Thus, above 0°C , the $f\text{O}_2$ of tochilinite
556 precipitation should be above the values estimated by Browning and Bourcier (1996). This
557 interpretation is supported by the high $\text{Fe}^{3+}/\Sigma\text{Fe}$ ratio measured in CM Paris Fe-rich tochilinite
558 (i.e., $8\text{--}15\%$; Pignatelli et al. 2017), suggesting that precipitation of tochilinite may have
559 occurred under sufficiently oxidizing conditions to incorporate Fe^{3+} into its mineral structure.
560 Consequently, CM tochilinite formation at $120\text{--}160^\circ\text{C}$ (**Fig. 13**) does not require such
561 extremely reduced conditions as at 0°C (Browning and Bourcier 1996). According to our S-
562 bearing experiments, the presence of a magnetite-like phase around iron metal grains suggests
563 $\log f\text{O}_2$ values between -73 and -60 at 80°C (**Fig. 13**).

564

CONCLUSIONS

565

566

567 We have performed low temperature experiments using starting mineral assemblages
568 (reduced glass, San Carlos olivine, metallic iron) close to those observed in the least altered
569 CM chondrites to better understand the alteration conditions of hydrated asteroids. Triangular
570 cronstedtite crystals formed only in S-free circumneutral conditions ($\text{pH} = 7\text{--}8$) with the
571 highest Fe content studied ($\text{Fe}_{\text{tot}}/\text{Si} = 2.7$), suggesting that chondritic cronstedtite crystals
572 likely formed by reaction of matrix amorphous silicates, Fe-Ni metal beads, and water. For
573 the first time, we have synthesized tochilinite similar to meteoritic tochilinite under conditions
574 analogous to CM chondrite alteration. Iron-rich tochilinite systematically surrounds iron
575 metal grains in all our S-bearing experiments, regardless of the starting mineral assemblage
576 and the proportion of metallic iron, indicating that chondritic tochilinite likely formed from
577 the alteration of Fe-Ni metal beads in a S-bearing alkaline environment at low temperature
578 (i.e., $< 160^\circ\text{C}$).

579 As both tochilinite and cronstedtite precipitated at 80°C in our experiments, these
580 minerals may have formed at similar aqueous alteration temperatures in CM chondrites.
581 Because cronstedtite stability field is expected to diminish with increasing temperature, an
582 expected co-precipitation of tochilinite and cronstedtite requires restrictive alteration
583 conditions: $80\text{--}120^\circ\text{C}$, $\text{pH} = 7\text{--}8$, and more oxidized conditions ($\log f\text{O}_2 \approx -65$ to -60) than
584 previously estimated for tochilinite. Comparison of our results to other experimental
585 approaches revealed a positive correlation between the Mg content in the hydroxide layer of
586 synthetic tochilinite and temperature. Based on this correlation, we estimated the mean
587 precipitation temperatures of meteoritic tochilinite to be $\sim 120^\circ\text{C}$ for Paris, $\sim 130^\circ\text{C}$ for
588 Murchison and Murray, $\sim 150^\circ\text{C}$ for Nogoya, and $\sim 160^\circ\text{C}$ for Cold Bokkeveld.

589

590 *Acknowledgments*—We are very grateful to Jaafar Ghanbaja and Sylvie Migot for assistance
591 with TEM characterization. We thank Hervé Marmier, Géraldine Kitzinger, and the SARM
592 team for their technical support for solution analyses. Maxime Clément is thanked for his
593 support in the reduction of the synthetic glass with the sealed evacuated silica glass tubes. We
594 are grateful to Pierrick Durant for his assistance with XRD analyses. We are also grateful to
595 Conel Alexander for very constructive review and helpful comments. Isabella Pignatelli is
596 thanked for helpful discussions. Roger Hewins, Martin Lee and associated editor Mike
597 Zolensky are thanked for constructive reviews and comments. This research was funded by

598 l'Agence Nationale de la Recherche through grant ANR-14-CE33-0002-01 SAPINS (PI Yves
599 Marrocchi) and OTELo. This is CRPG contribution #2676.

600

601

REFERENCES

602 Barber D. J. 1981. Matrix phyllosilicates and associated minerals in C2M carbonaceous
603 chondrites. *Geochimica et Cosmochimica Acta* 45:945–970.

604 Bailey S. W. 1988. Odinite, a new dioctahedral-trioctahedral Fe³⁺-rich 1:1 clay mineral. *Clay*
605 *Mineral* 23:237-247.

606 Bunch T. E. and Chang S. 1980. Carbonaceous chondrites-II. Carbonaceous chondrite
607 phyllosilicates and light element geochemistry as indicators of parent body processes
608 and surface conditions. *Geochimica et Cosmochimica Acta* 44:1543–1577.

609 Benedix G., Leshin L., Farquhar J., Jackson T., and Thiemens M. 2003. Carbonates in CM2
610 chondrites: constraints on alteration conditions from oxygen isotopic compositions
611 and petrographic observations. *Geochimica et Cosmochimica Acta* 67:1577–1588.

612 Bradley, J. P. 1994. Chemically Anomalous, Preaccretionally Irradiated Grains in
613 Interplanetary Dust from Comets. *Science* 265:925-929.

614 Brearley A. J. 2006. The action of water. In *Meteorites and the early solar system II*, edited
615 by Lauretta D. S. and McSween H. Y. Tucson, Arizona: The University of Arizona
616 Press. pp. 587–624.

617 Brindley, G.W. 1982. Chemical compositions of berthierines – a review. *Clays Clay Miner.*
618 30:153–155.

619 Browning L. B. and Bourcier W. L. 1996. Tochilinite: A sensitive indicator of alteration
620 conditions on the CM asteroidal parent body. Proceedings, 44th Lunar and Planetary
621 Science Conference. pp. 171–172.

622 Chistyakova N.I., Rusakov V.S., Gubaidulina T.V., and Kozerenko S.V. 2006. Investigations
623 of sulfide minerals with layered structure by Mössbauer spectroscopy methods.
624 *ICAME 2005* 66:613–617.

625 Clark B. E., Ziffer J., Nesvornyy D., Campins H., Rivkin A. S., Hiroi T., Barucci M. A.,
626 Fulchignoni M., Binzel R. P., Fornasier S., DeMeo F., Ockert-Bell M. E., Licandro J.,
627 and Mothé-Diniz T. 2010. Spectroscopy of B-type asteroids: Subgroups and meteorite
628 analogs. *Journal of Geophysical Research Planets* 115:1-22.

629 Clayton R. N. and Mayeda T. K. 1984. The oxygen isotope record in Murchison and other
630 carbonaceous chondrites. *Earth and Planetary Science Letter* 67:151–161.

631 Cloutis E. A., Hiroi T., Gaffey M. J., Alexander C. M. O'D., and Mann P. 2011. Spectral
632 reflectance properties of carbonaceous chondrites: 1. CI chondrites. *Icarus* 212:180–
633 209.

634 Dargent M., Truche L., Dubessy J., Bessaque G., and Marmier H. 2015. Reduction Kinetics

- 635 of Aqueous U(VI) in Acidic Chloride Brines to Uraninite by Methane, Hydrogen or C-
636 Graphite under Hydrothermal Conditions: Implications for the Genesis of
637 Unconformity-Related Uranium Ore Deposits. *Geochimica et Cosmochimica Acta*
638 167:11–26.
- 639 Davoisne C., Djouadi Z., Leroux H., d’Hendecourt L., Jones A., and Deboffle D. 2006. The
640 origin of GEMS in IDPs as deduced from microstructural evolution of amorphous
641 silicates with annealing. *Astronomy & Astrophysics* 448:L1-L4.
- 642 Declercq J., Diedrich T., Perrot M., Gislason S. R., and Oelkers E. H. 2013. Experimental
643 determination of rhyolitic glass dissolution rates at 40–200°C and $2 < \text{pH} < 10.1$.
644 *Geochimica et Cosmochimica Acta* 100:251–263.
- 645 Dyl K.A., Manning C.E., and Young E.D. 2006. Modelling aqueous alteration of CM
646 carbonaceous chondrites: implications for cronstedtite formation by water-rock
647 reaction. (abstract #2060). 37th Lunar and Planetary Science Conference.
- 648 Fuchs L. H., Olsen E., and Jensen K. J. 1973. Mineralogy, mineral-chemistry, and
649 composition of the Murchison (C2) meteorite. *Smithsonian Contributions to the Earth*
650 *Sciences* 10:1–39.
- 651 Fujiya W., Sugiura N., Marrocchi Y., Takahata N., Hoppe P., Shirai K., Sano Y., and
652 Hiyaogon H. 2015. Comprehensive study of carbon and oxygen isotopic compositions,
653 trace element abundances, and cathodoluminescence intensities of calcite in the
654 Murchison CM chondrite. *Geochimica et Cosmochimica Acta* 161:101–117.
- 655 Gubaidulina T. V., Chistyakova N. I., and Rusakov V. S. 2007. Mössbauer study of layered
656 iron hydroxysulfides: Tochilinite and valleriite. *Bulletin of the Russian Academy of*
657 *Sciences: Physics* 71:1269–1272.
- 658 Guggenheim S., Bailey S. W., Eggleton R. A., and Wilkes P. 1982. Structural aspects of
659 greenalite and related minerals. *The Canadian Mineralogist* 20:1-18.
- 660 Haack H., Grau T., Bischoff A., Horstmann M., Wasson J., Sorensen A., Laubenstein M., Ott
661 U., Palme H., Gellissen M., Greenwood R. C., Pearson V. K., Franchi I. A., Gabelica
662 Z., and Schmitt-Kopplin P. 2012. Maribo-A new CM fall from Denmark. *Meteoritics*
663 *& Planetary Science* 47:30-50.
- 664 Hanowski N. P. and Brearley A. J. 2001. Aqueous alteration of chondrules in the CM
665 carbonaceous chondrite, Allan Hills 81002: Implications for parent body alteration.
666 *Geochimica et Cosmochimica Acta* 65:495–518.
- 667 Hewins R. H., Bourot-Denise M., Zanda B., Leroux H., Barrat J.-A., Humayun M., Göpel C.,
668 Greenwood R. C., Franchi I. A., Pont S., Lorand J.-P., Cournède C., Gattacceca J.,
669 Rochette P., Kuga M., Marrocchi Y., and Marty B. 2014. The Paris meteorite, the least
670 altered CM chondrite so far. *Geochimica et Cosmochimica Acta* 124:190–222.
- 671 Holland H. D. 1959. Stability relations among the oxides, sulfides, sulfates and carbonates of
672 ore and gangue metals, [Part] 1 of Some applications of thermochemical data to
673 problems of ore deposits. *Economic Geology* 54:184–233.
- 674 Howard K. T., Alexander C. M. O’D., Schrader D. L., and Dyl K. A. 2015. Classification of

- 675 hydrous meteorites (CR, CM and C2 ungrouped) by phyllosilicate fraction: PSD-XRD
676 modal mineralogy and planetesimal environments. *Geochimica et Cosmochimica Acta*
677 149:206–222.
- 678 Howard K. T., Benedix G. K., Bland P. A. and Cressey G. 2011. Modal mineralogy of CM
679 chondrites by X-ray diffraction (PSD-XRD): Part 2. Degree, nature and settings of
680 aqueous alteration. *Geochimica et Cosmochimica Acta* 75:2735–2751.
- 681 Howard K. T., Benedix G. K., Bland P. A. and Cressey G. 2009. Modal mineralogy of CM2
682 chondrites by PSD-XRD: Part 1. Total phyllosilicate abundance and the degree of
683 aqueous alteration. *Geochimica et Cosmochimica Acta* 73:4576–4589.
- 684 Hybler J., Petříček V., Ďurovič S., and Smrčok Ľ. 2000. Refinement of the Crystal Structure
685 of Cronstedtite-1T. *Clays and Clay Minerals* 48:331–338.
- 686 Jarosewich E. 1990. Chemical analyses of meteorites: a compilation of stony and iron
687 meteorite analyses. *Meteoritics* 25:323–337.
- 688 Kakos G. A., Turney T. W., and Williams T. B. 1994. Synthesis and structure of tochilinite: A
689 layered metal hydroxide/sulfide composite. *Journal of Solid State Chemistry* 108:102–
690 111.
- 691 Keller L. P. and Messenger S. 2011. On the origins of GEMS grains. *Geochimica et*
692 *Cosmochimica Acta* 75:5336–5365.
- 693 Kogure, T., Hybler, J., and Yoshida, H. 2002. Coexistence of two polytypic groups in
694 cronstedtite from Lostwithiel England. *Clays and Clay Minerals* 50:504-513.
- 695 Kozerenko S.V., Fadeev V.V., Organova N.I., Chstyakova N.I., Kolpakova N.N., and Senin
696 V.G. 2001. Synthesis, formation conditions and crystallochemistry of tochilinites –
697 iron, magnesium and sodium hydroxide-sulfides. *Experiment in Geosciences* 10:57-
698 58.
- 699 Kozerenko S. V., Organova N. J., Fadeev V. V., Magazina L.O., Kolpakova N. N., and
700 Kopneva L. A. 1996. Tochilinite produced in laboratory. Proceedings, 27th Lunar and
701 Planetary Science Conference. pp. 695–696.
- 702 Lanson, B., Lantenois, S., Van Aken, P.A., Bauer, A., and Plançon, A. 2012. Experimental
703 investigation of smectite interaction with metal iron at 80°C: structural
704 characterization of newly formed Fe-rich phyllosilicates. *American Mineralogist*
705 97:864-871.
- 706 Lantenois, S., Lanson, B., Muller, F., Bauer, A., Jullien, M., and Plançon, A. 2005.
707 Experimental study of smectite interaction with metal Fe at low temperature: 1.
708 Smectite destabilization. *Clays and Clay Minerals* 53:597-612.
- 709 Lee M. R., Lindgren P. and Sofe M. R. 2014. Aragonite, breunnerite, calcite and dolomite in
710 the CM carbonaceous chondrites: High fidelity recorders of progressive parent body
711 aqueous alteration. *Geochimica et Cosmochimica Acta* 144:126–156.
- 712 Lee M. R., Sofe M. R., Lindgren P., Starkey N. A. and Franchi I. A. 2013. The oxygen
713 isotope evolution of parent body aqueous solutions as recorded by multiple carbonate

- 714 generations in the Lonewolf Nunatak 94101 CM2 carbonaceous chondrite.
715 *Geochimica et Cosmochimica Acta* 121:452–466.
- 716 Lee M. R. and Ellen R. 2008. Aragonite in the Murray (CM2) carbonaceous chondrite:
717 implications for parent body compaction and aqueous alteration. *Meteoritics &*
718 *Planetary Science* 43:1219–1231.
- 719 Leroux H., Cuvillier P., Zanda B., and Hewins R. H. 2015. GEMS-like material in the matrix
720 of the Paris meteorite and the early stages of alteration of CM chondrites. *Geochimica*
721 *et Cosmochimica Acta* 170:247–265.
- 722 MacKinnon I. D. R. and Zolensky M. E. 1984. Proposed structures for poorly characterized
723 phases in C2M carbonaceous chondrite matrix. *Nature* 309:240–242.
- 724 Marrocchi Y., Gounelle M., Blanchard I., Caste F. and Kearsley A. T. (2014) The Paris CM
725 chondrite: Secondary minerals and asteroidal processing. *Meteorit. Planet. Sci.* **49**,
726 1232–1249.
- 727 Marrocchi Y., Bekaert D. V., and Piani L. 2018. Origin and abundance of water in
728 carbonaceous asteroids. *Earth and Planetary Science Letter* 482:23–32.
- 729 McAlister, J.A. and Kettler, R.M. 2008. Metastable equilibria among dicarboxylic acids and
730 the oxidation state during aqueous alteration on the CM2 chondrite parent body.
731 *Geochimica et Cosmochimica Acta* 72:233-241.
- 732 Mizutani T., Fukushima Y., Okada A., Kamigaito, O., and Kobayashi T. 1991. Synthesis of
733 1:1 and 2:1 iron phyllosilicates and characterization of their iron state by Mössbauer
734 spectroscopy. *Clays and Clay Minerals* 39:381–386.
- 735 Moroz L. V., Kozerenko S. V. and Fadeev V. V. 1997. The reflectance spectrum of synthetic
736 tochilinite. Proceedings, 28th Lunar and Planetary Science Conference. pp. 983-984.
- 737 Nakamura T. and Nakamuta Y. 1996. X-ray study of PCP from the Murchison CM
738 carbonaceous chondrite. *Proceeding of the NIPR Symposium on Antarctic Meteorites*
739 9:37–50.
- 740 Organova N. I., Gorshkov A. I., Dikov Yu. P., Kul'bachinskiy V. A., Laputina I. P., Sivtsov
741 A. V., Sluzhenikin S. F., and Ponomarenko A. I. 1988. The new data on tochilinite.
742 *International Geology Review* 6:84–98.
- 743 Organova N. I., Drits V. A., and Dmitrik A. L. 1973. Structural study of tochilinite. Part I.
744 The isometric variety. *Soviet Physics - Crystallography* 17:667-671.
- 745 Organova N. I., Genkin A. D., Drits V. A., Dmitrik A. L. and Kuzmina O. V. 1971.
746 Tochilinite: A new sulfide hydroxide of iron and magnesium. *Zapiski Vses*
747 *Mineralogiscogo Obschestva* 4:477-487.
- 748 Palmer E. E. and Lauretta D. S. 2011. Aqueous alteration of kamacite in CM chondrites.
749 *Meteoritics & Planetary Science* 46:1587–1607.
- 750 Peng Y., Xu L., Xi G., Zhong C., Lu J., Meng Z., Li G., Zhang S., Zhang G., and Qian Y.
751 2007. An experimental study on the hydrothermal preparation of tochilinite nanotubes

- 752 and tochilinite serpentine-intergrowth nanotubes from metal particles. *Geochimica et*
753 *Cosmochimica Acta* 71:2858–2875.
- 754 Peng Y. and Jing Y. 2014. Hydrothermal preparation of analogous matrix materials of
755 carbonaceous chondrites from metal alloy particles. *Meteoritics & Planetary Science*
756 402:252-262.
- 757 Pierron O. 2011. Interactions eau-fer-argilite: Rôle des paramètres Liquide/Roche,
758 Fer/Argilite, Température sur la nature des phases minérales. Ph.D. thesis, Henri
759 Poincaré University, Nancy, France.
- 760 Pekov I. V., Sereda E. V., Polekhovsky Yu. S., Britvin S. N., Chukanov N. V., Yapaskurt V.
761 O., and Bryzgalov I. A. 2013. Ferrotchilinite, $6\text{FeS} \cdot 5\text{Fe}(\text{OH})_2$, a new mineral from
762 the Oktyabr'sky deposit, Noril'sk district, Siberia, Russia. *Geology of Ore Deposits*
763 55:567-574.
- 764 Pignatelli I., Mugnaioli E., and Marrocchi Y. 2018. Cronstedtite polytypes in the Paris
765 meteorite. *European Journal Mineralogy* 30:349-354.
- 766 Pignatelli I., Marrocchi Y., Mugnaioli E., Bourdelle F., and Gounelle M. 2017. Mineralogical,
767 crystallographic and redox features of the earliest stages of fluid alteration in CM
768 chondrites. *Geochimica et Cosmochimica Acta* 209:106–122.
- 769 Pignatelli I., Marrocchi Y., Vacher L. G., Delon R., and Gounelle M. 2016. Multiple
770 precursors of secondary mineralogical assemblages in CM chondrites. *Meteoritics &*
771 *Planetary Science* 51:785–805.
- 772 Pignatelli I., Vacher L. G., and Marrocchi Y. 2015. Hydrothermal preparation of analogous
773 matrix minerals of CM carbonaceous chondrites from metal alloy particles” by Y.
774 Peng and Y.Jing [Earth Planet. Sci. Lett. 408 (2014) 252–262]. *Earth and Planetary*
775 *Science Letter* 428:307–309.
- 776 Pignatelli I., Bourdelle F., Bartier D., Mosser-Ruck R., Truche L., Mugnaioli E., and Michau
777 N. 2014. Iron-clay interactions: detailed study of the mineralogical transformation of
778 claystone with emphasis on the formation of iron-rich T-O phyllosilicates in a step-by-
779 step cooling experiment from 90°C to 40°C. *Chemical Geology* 387:1-11.
- 780 Pignatelli I., Mugnaioli E., Hybler J., Mosser-Ruck R., Cathelineau M., and Michau N. 2013.
781 A multi-technique characterization of cronstedtite synthesized by iron–clay interaction
782 in a step-by-step cooling procedure. *Clays and Clay Minerals* 61:277–289.
- 783 Ramdohr P. 1963. The opaque minerals in stony meteorites. *Journal of Geophysical Research*
784 68:2011–2036.
- 785 Rivard, C. 2011. Contribution à l'étude de la stabilité des minéraux constitutifs de l'argilite du
786 Callovo-Oxfordien en présence de fer à 90°C. Ph.D. thesis, Henri Poincaré University,
787 Nancy, France.
- 788 Rubin A. E., Trigo-Rodríguez J. M., Huber H., and Wasson J. T. 2007. Progressive aqueous
789 alteration of CM carbonaceous chondrites. *Geochimica et Cosmochimica Acta*
790 71:2361–2382.

- 791 Schulte, M. and Schock, E. 2004. Coupled organic synthesis and mineral alteration on the
792 meteorite parent bodies. *Earth and Planetary Science Letter* 39:1577-1590.
- 793 Skynner, B. J. and Luce, D. 1971. Solid Solutions of the type (Ca,Mg,Mn,Fe)S and their use
794 as geothermometers for the enstatite chondrites. *American Mineralogist* 56:1269-
795 1297.
- 796 Tomeoka K. and Buseck P. R. 1985. Indicators of aqueous alteration in CM carbonaceous
797 chondrites: Microtextures of a layered mineral containing Fe, S, O and Ni.
798 *Geochimica et Cosmochimica Acta* 49:2149–2163.
- 799 Vacher L. G., Marrocchi Y., Villeneuve J., Verdier-Paoletti M. J., and Gounelle M. 2017.
800 Petrographic and C & O isotopic characteristics of the earliest stages of aqueous
801 alteration of CM chondrites. *Geochimica et Cosmochimica Acta* 213:271–290.
- 802 Velbel M. A. 2014. Stoichiometric reactions describing serpentinization of anhydrous primary
803 silicates: a critical appraisal, with application to aqueous alteration of chondrule
804 silicates in CM carbonaceous chondrites. *Clays and Clay Minerals* 62:126-136.
- 805 Verdier-Paoletti M. J., Marrocchi Y., Avice G., Roskosz M., Gurenko A. and Gounelle M.
806 (2017) Oxygen isotope constraints on the alteration temperatures of CM chondrites.
807 *Earth Planet. Sci. Lett.* **458**, 273–281.
- 808 Vienna, J. D., James J. N., Joseph V. R., and Sebastien N. K. 2018. Impacts of glass
809 composition, pH, and temperature on glass forward dissolution rate. *Npj Materials*
810 *Degradation* 2:22.
- 811 Zolensky M. E., Mittlefehldt D. W., Lipschutz M. E., Wang M.-S., Clayton R. N., Mayeda T.
812 K., Grady M. M., Pillinger C., and B D. 1997. CM chondrites exhibit the complete
813 petrologic range from type 2 to 1. *Geochimica et Cosmochimica Acta* 61:5099–5115.
- 814 Zolensky M. E. and Mackinnon I. D. R. 1986. Microstructures of cylindrical tochilinites.
815 *American Mineralogist* 71:1201–1209.
- 816 Zolensky M. E., Barrett R. and Browning L. 1993. Mineralogy and composition of matrix and
817 chondrule rims in carbonaceous chondrites. *Geochimica et Cosmochimica Acta*
818 57:3123–3148.
- 819 Zolotov M. Y. 2014. Formation of brucite and cronstedtite-bearing mineral assemblages on
820 Ceres. *Icarus* 228:13–26.

821

FIGURE CAPTIONS

822
823
824 **Fig. 1.** Synthetic GEMS-like glass preparation. a) Schematic representation of the sealed
825 evacuated silica tube method used in this study to reduce our synthetic glass. At time t_1 , the
826 silica glass tube was connected to a vacuum pump to evacuate the atmosphere inside the tube.
827 When the pressure reached 2×10^{-2} mbar (time t_2), the silica glass was melted using a torch to
828 seal the tube without breaking the vacuum. b) and c) BSE images of the synthetic GEMS-like
829 material after three days of reduction at 1000°C .

830
831 **Fig. 2.** Overview of the anoxic hydrothermal experiments. a) Initial mixing proportions of the
832 solid starting products and their respective bulk Fe/Si ratio. b) Schematic representation of the
833 loaded autoclaves for the two sets of experiments and summary of the initial parameters.

834
835 **Fig. 3.** Run products from the circumneutral S-free experiments. a) BSE image of run
836 products from experiment GOI-2, showing the occurrence of iron oxide grains of a few tens
837 of microns. b) TEM imaging of a Fe-Si-rich phase located around an iron metal grain in
838 experiment G-1. c) Chemical compositions (wt.%) of the synthetic assemblages produced in
839 experiments GOI-1 and GOI-2 plotted in a Fe-Mg-Si ternary diagram (see Table S1 for
840 details). White diamonds represent the composition of meteoritic cronstedtite from the Paris
841 CM chondrite (Pignatelli et al. 2018). Black circles represent the ideal chemical compositions
842 of berthierine ('Be'; Brindley 1982), cronstedtite ('Cr'; Hybler et al. 2000; Pignatelli et al.
843 2013), greenalite ('Gr'; Guggenheim et al. 1982), kamacite ('Ka'), and odinite ('Od'; Bailey
844 1988).

845
846 **Fig. 4.** TEM images and SAED patterns of run products from neutral S-free experiment GOI-
847 2. a) An aggregate of four cronstedtite crystals. b) A single cronstedtite crystal in direct
848 contact with fibrous Fe-rich phyllosilicate. c) and d) TEM image and corresponding SAED
849 pattern along the [001] zone axis of a synthetic cronstedtite. e) and f) TEM image and
850 corresponding SAED pattern along the [010] zone axis of another cronstedtite.

851
852 **Fig. 5.** Evolution of solution chemistry during neutral S-free experiments a) G, b) GO, and c)
853 GOI. Si (magenta), Ca (green), Mg (purple), and Fe (orange) concentrations in the run
854 solutions are shown as a function of elapsed time (error bars are 10%). Al concentrations (not
855 shown) remained low and are reported in **Table S2**. d) pH of the solutions measured at 25°C

856 in experiments G (black open squares and solid line), GO (black solid squares and dashed
857 line), and GOI (gray solid squares and line) shown as a function of elapsed time.

858

859 **Fig. 6.** Run products from alkaline S-bearing experiments. a) and b) BSE images of iron metal
860 beads surrounded by three layers of newly precipitated assemblages in experiment GOS-1.
861 These phases show different textures: (i) an inner compact layer, (ii) an intermediate acicular
862 layer, and (iii) an outer fibrous layer of variable thickness. c) Chemical compositions (wt.%)
863 of the synthetic assemblages produced in experiments G-S and GO-S plotted in a Fe-S-Si
864 ternary diagram (see Table S3 for details). Black circles represent the ideal chemical
865 compositions of cronstedtite ('Cr'; Hybler et al. 2000; Pignatelli et al. 2013), ferrotachilinite
866 ('Fe-To'; Pekov et al. 2013), greenalite ('Gr'; Guggenheim et al. 1982), kamacite ('Ka), and
867 Mg-tochilinite ('Mg-To'; Organova et al. 1971).

868

869 **Fig. 7.** TEM characterization of secondary iron oxide layers around iron metal grains in
870 alkaline S-bearing experiments. a) An iron metal grain from the FIB-produced cross section
871 of samples from experiment GS-2, surrounded by three layers (Z_1 , Z_2 , and Z_3) of secondary
872 assemblages. The white solid line in (a) represents the location of the TEM chemical profile
873 in (e). b) to d) TEM-EDS maps of Si, Fe, and S distributions in the same area shown in (a). e)
874 TEM chemical profile of Fe, O, S, and Si concentrations corresponding to the white solid line
875 in (a).

876

877 **Fig. 8.** TEM images and SAED patterns of secondary acicular tochilinite around iron metal
878 grains. a) TEM image of the GOS-2 FIB-produced cross section. B) TEM image of the
879 products of the S-bearing experiment around an iron metal bead. c) TEM image of the Fe-S-
880 rich acicular layer from the GS-2 FIB-produced cross section. d) SAED pattern collected from
881 the acicular mineral displayed in (c) showing broad rings of varying intensity that are
882 consistent with natural tochilinite (Organova et al. 1973; Pekov et al. 2013). e) HRTEM
883 image of a acicular tochilinite. f) SAED pattern of tochilinite along the c^* axis showing the
884 strong (002) diffraction spots of tochilinite.

885

886 **Fig. 9.** Evolution of solution chemistry during alkaline S-bearing experiments a) GS, b) GOS,
887 and c) GOIS. Si (magenta) and Ca (green) concentrations of the solutions are shown as a
888 function of elapsed time (errors are 10%). Mg, Al, and Fe concentrations (not shown)
889 remained very low and are reported in **Table 2**. d) pH of solutions measured at 25°C in

890 experiments GS (black open squares and solid line), GOS (black solid squares and dashed
891 line), and GOIS (grey solid squares and solid line) shown as a function of elapsed time.

892

893 **Fig. 10.** The stability fields of cronstedtite, greenalite, hematite, and magnetite in $\log [\text{Si}_{(\text{aq})}]$
894 vs $f(\text{O}_2)$ phase diagrams at 80°C (solid black line and blue shaded field), 100°C, and 150°C
895 (dotted lines) from Pignatelli et al. 2014. The vertical dashed black line corresponds to the Si
896 concentration measured in the run solution of S-free experiment GOI and the red shaded area
897 represents the range of Si concentrations measured in the solutions of S-bearing experiment
898 GOIS.

899

900 **Fig. 11.** Synthesis temperature as a function of Mg content (nMg) in synthetic tochilinite from
901 this study (red circle) and literature (black circles) (**Table S4**; Kakos et al. 1994; Kozerenko et
902 al. 1996, 2001; Chistyakova et al. 2006; Peng and Jing 2014). The blue shaded area represents
903 the nMg values of meteoritic tochilinite (Palmer and Lauretta 2011; Pignatelli et al. 2017) and
904 the associated formation temperatures based on the regression equation $T = 175.9 (\pm 44.6) \times$
905 $\text{nMg} + 100.4 (\pm 17.3)$.

906

907 **Fig. 12.** Schematic representation of the expected of ^{26}Al temperature profile of CM chondrite
908 parent body as function of time. The range of temperature formation of calcite (0-70°C, green
909 rectangle) and cronstedtite (50-120°C, blue rectangle) have been taken from the literature
910 (calcite: Clayton and Mayeda 1984, Benedix et al. 2003; Guo and Eiler 2007; cronstedtite:
911 Pignatelli et al. 2013, 2014; Zolotov 2014). Formation age of calcite from Fujiya et al. 2012 is
912 given as indication.

913

914 **Fig. 13.** $\log f\text{O}_2$ - $\log f\text{S}_2$ diagram of the Fe-O-S system at 80°C (solid line) and 25°C (dotted
915 line) demonstrating the co-stability field of tochilinite and cronstedtite, modified after Holland
916 (1959). The stability field of tochilinite at 0°C is from Browning and Bourcier (1996).

917

918
919
920

FIGURES

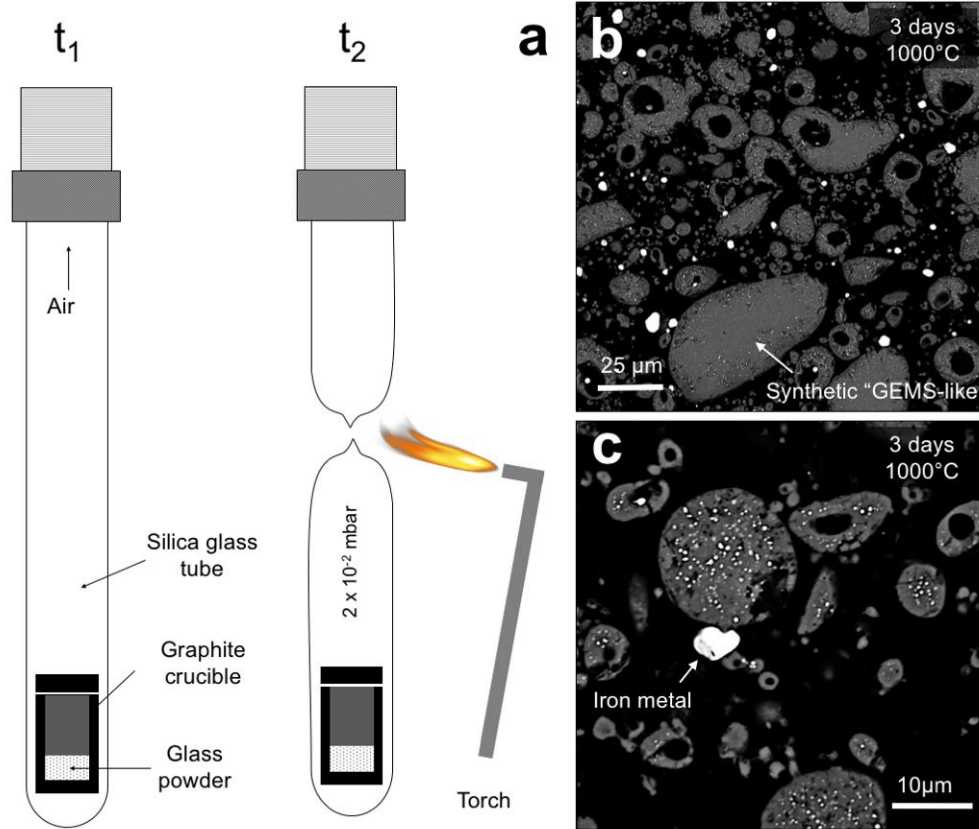


Figure 1

921
922
923

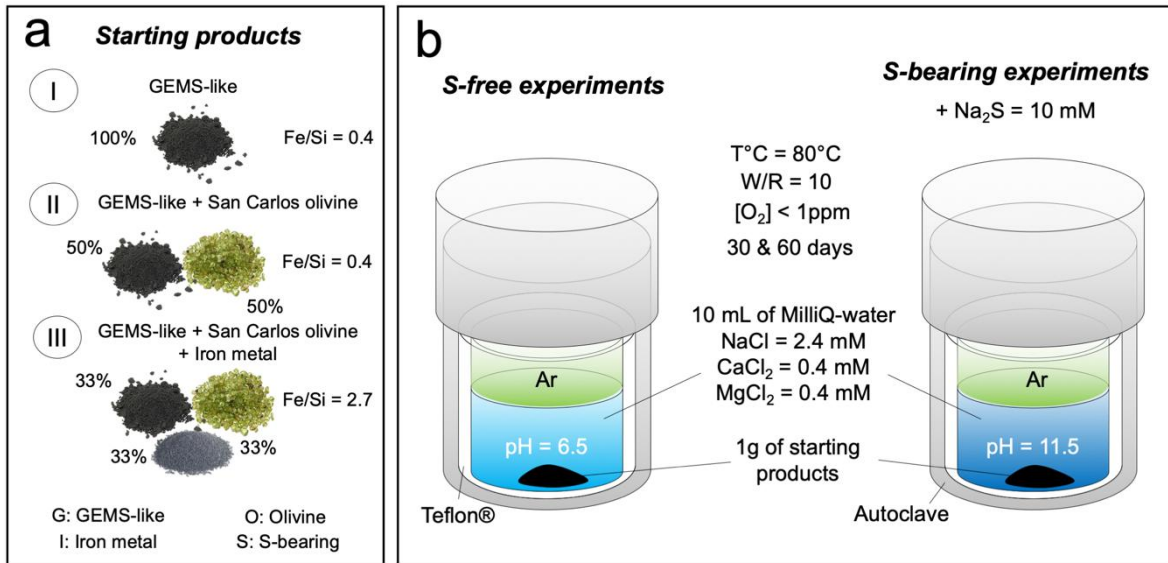


Figure 2

924
925
926

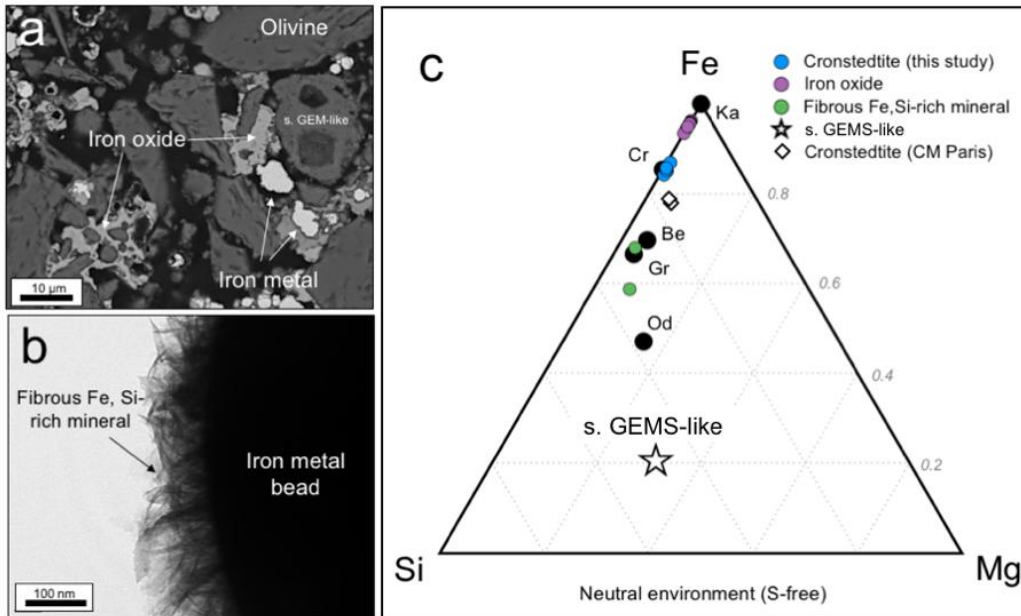


Figure 3

927
928
929

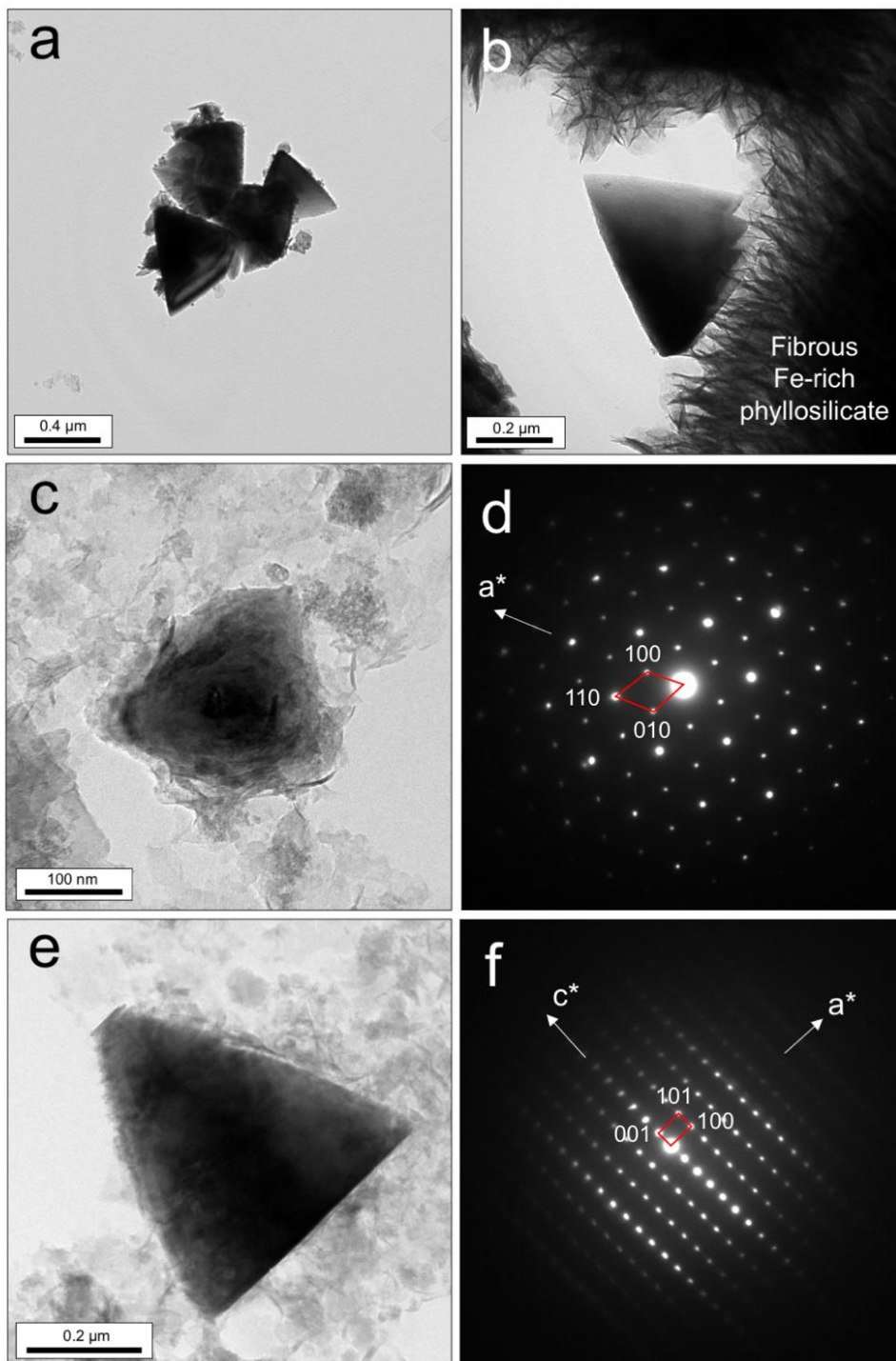


Figure 4

930
931
932

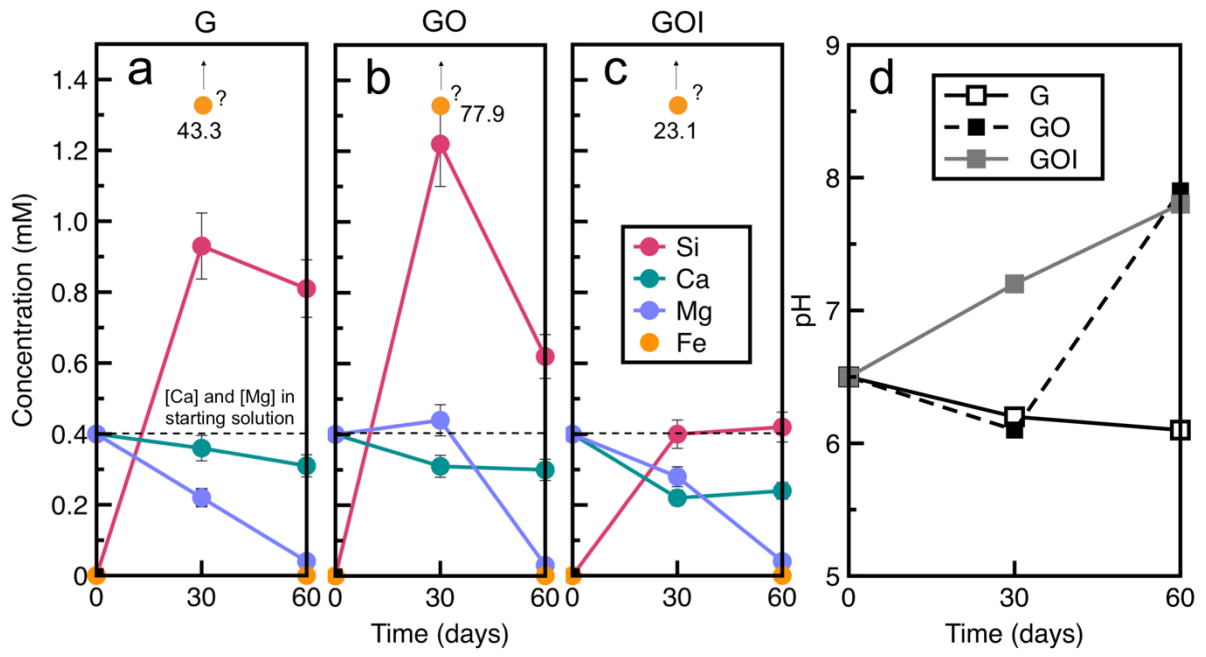


Figure 5

933
934
935
936

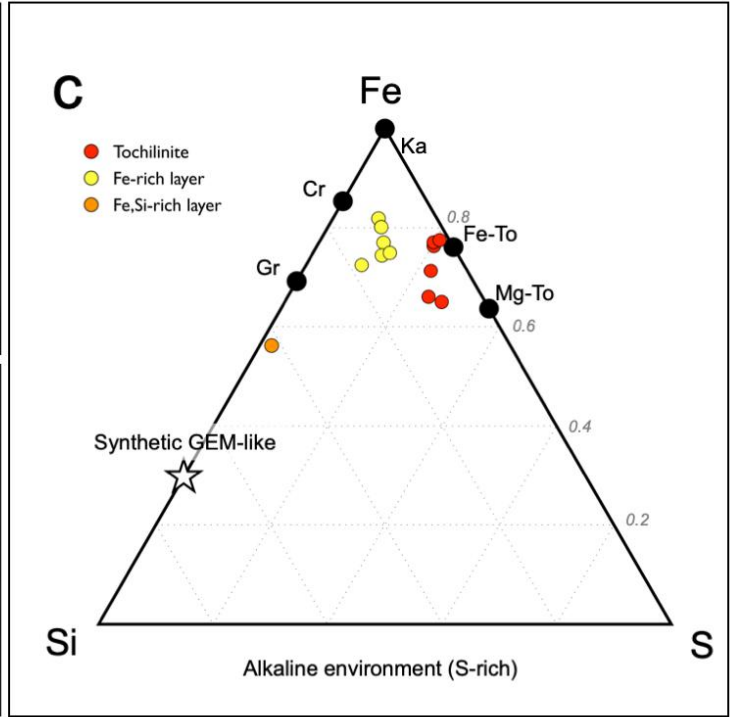
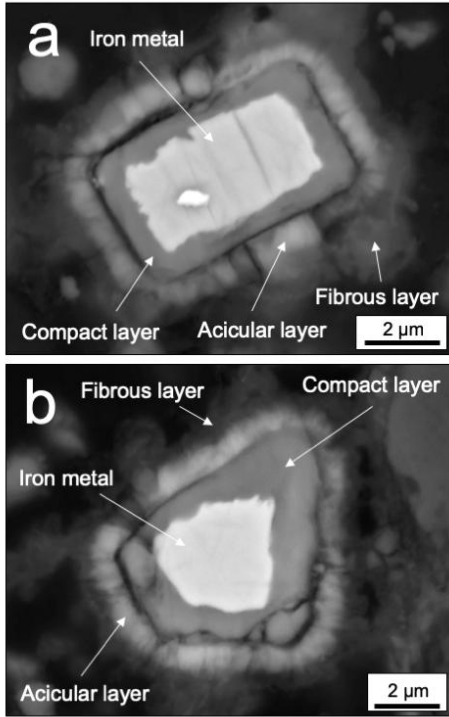


Figure 6

937
938
939

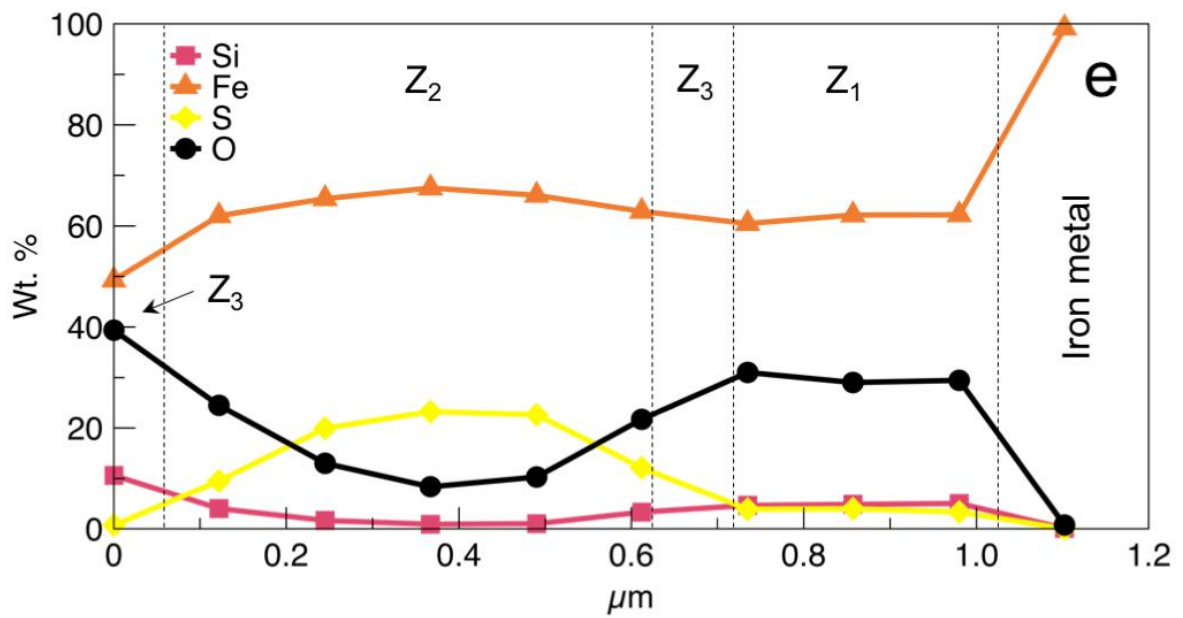
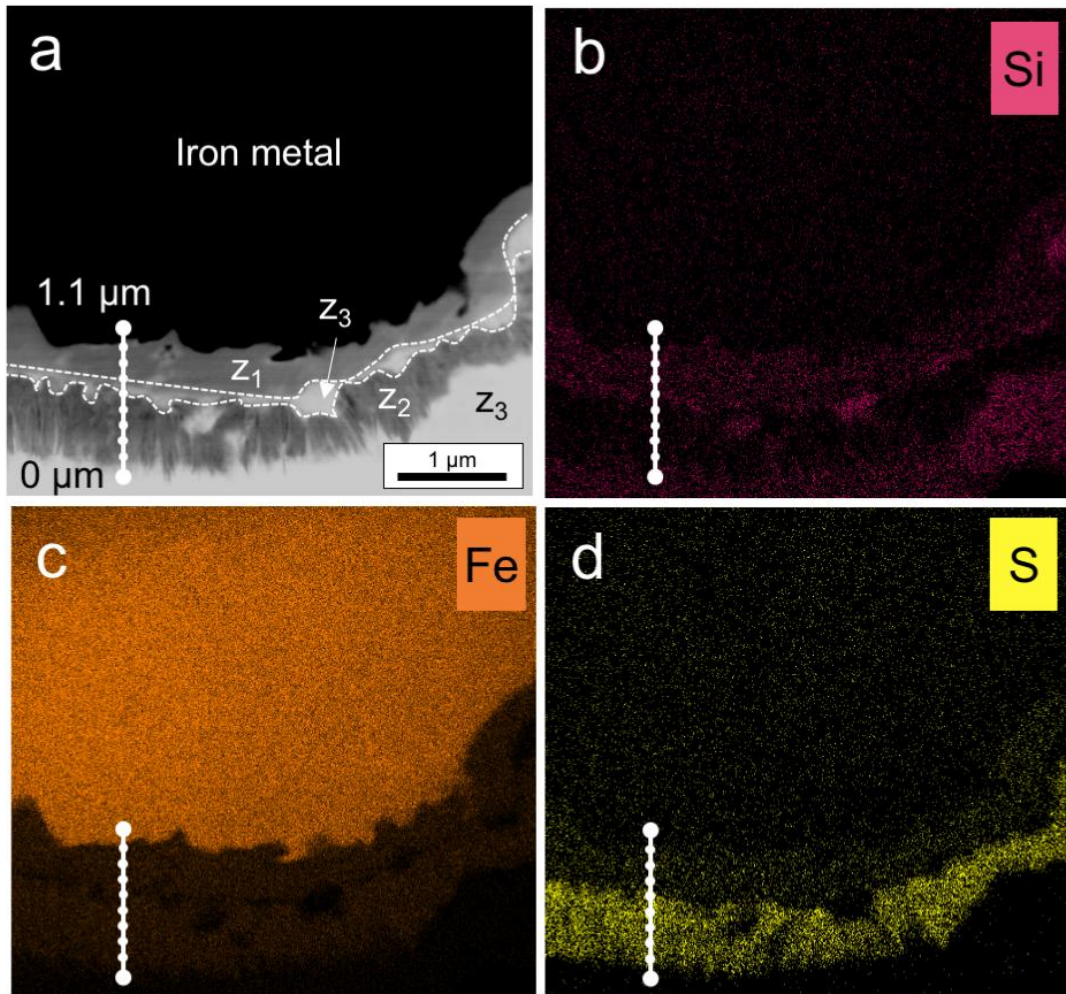


Figure 7

940
941
942

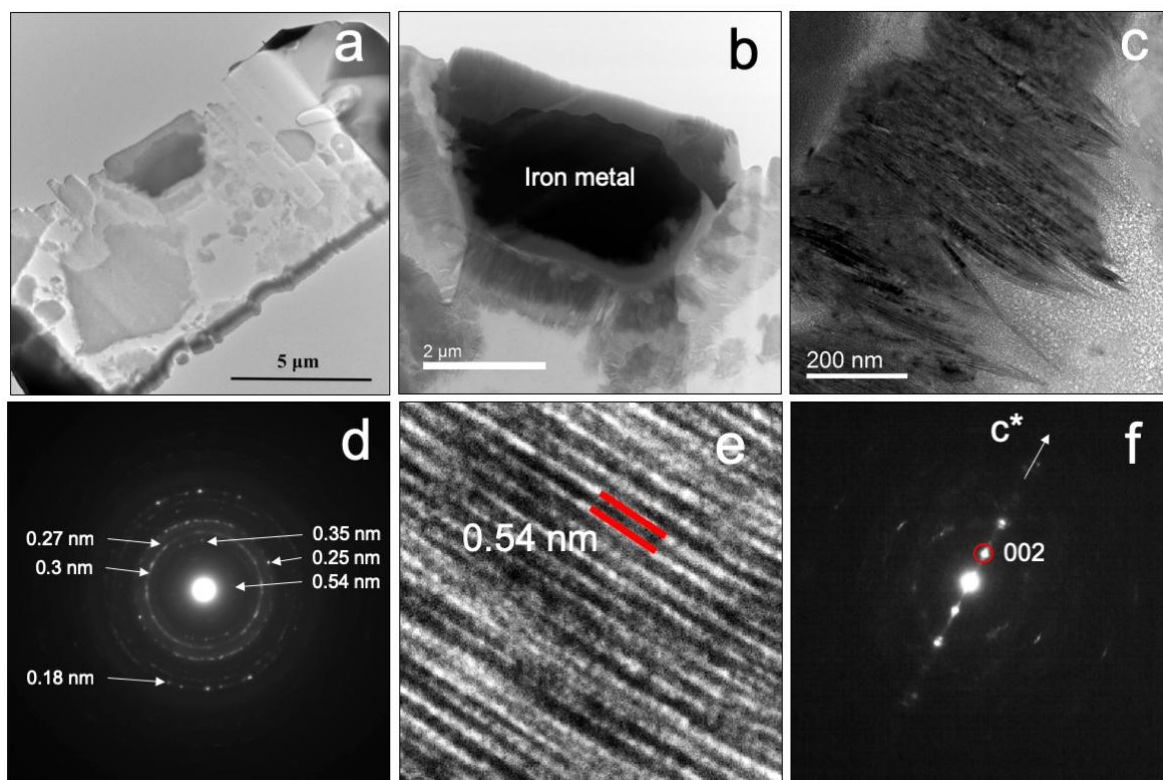


Figure 8

943
 944
 945
 946

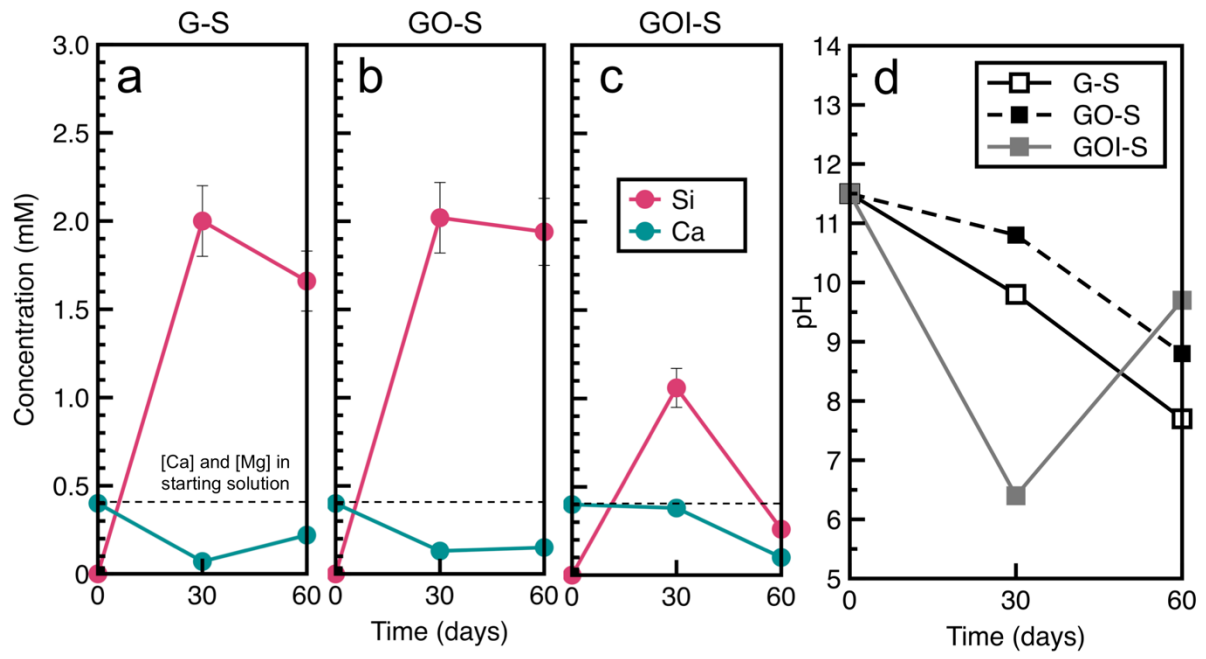


Figure 9

947
948
949
950

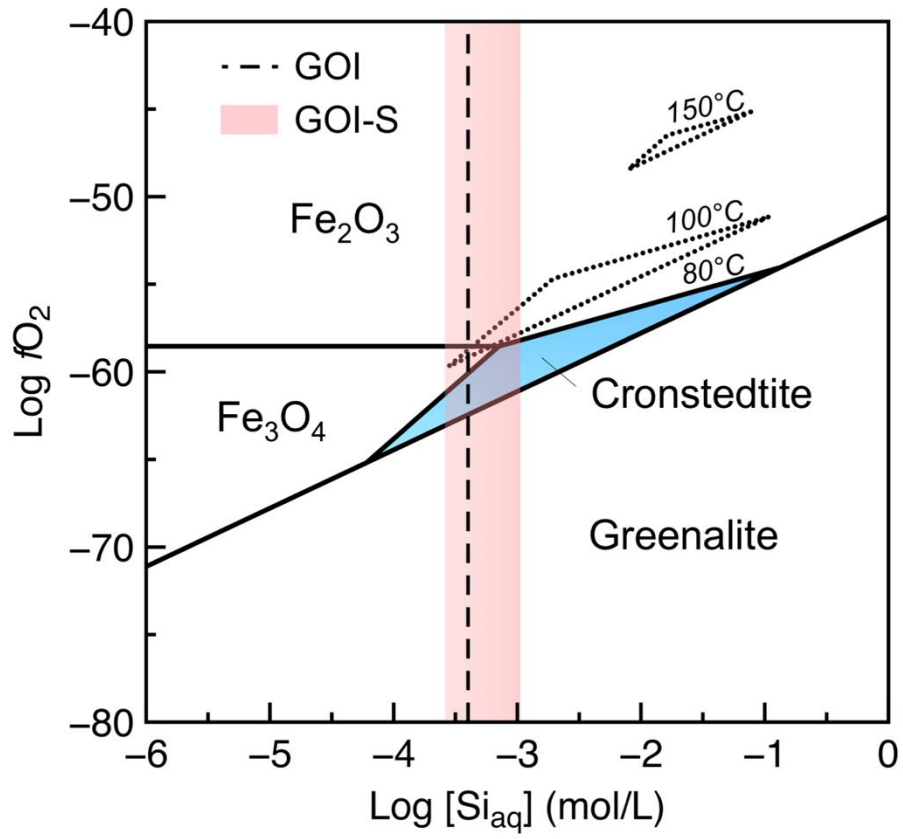
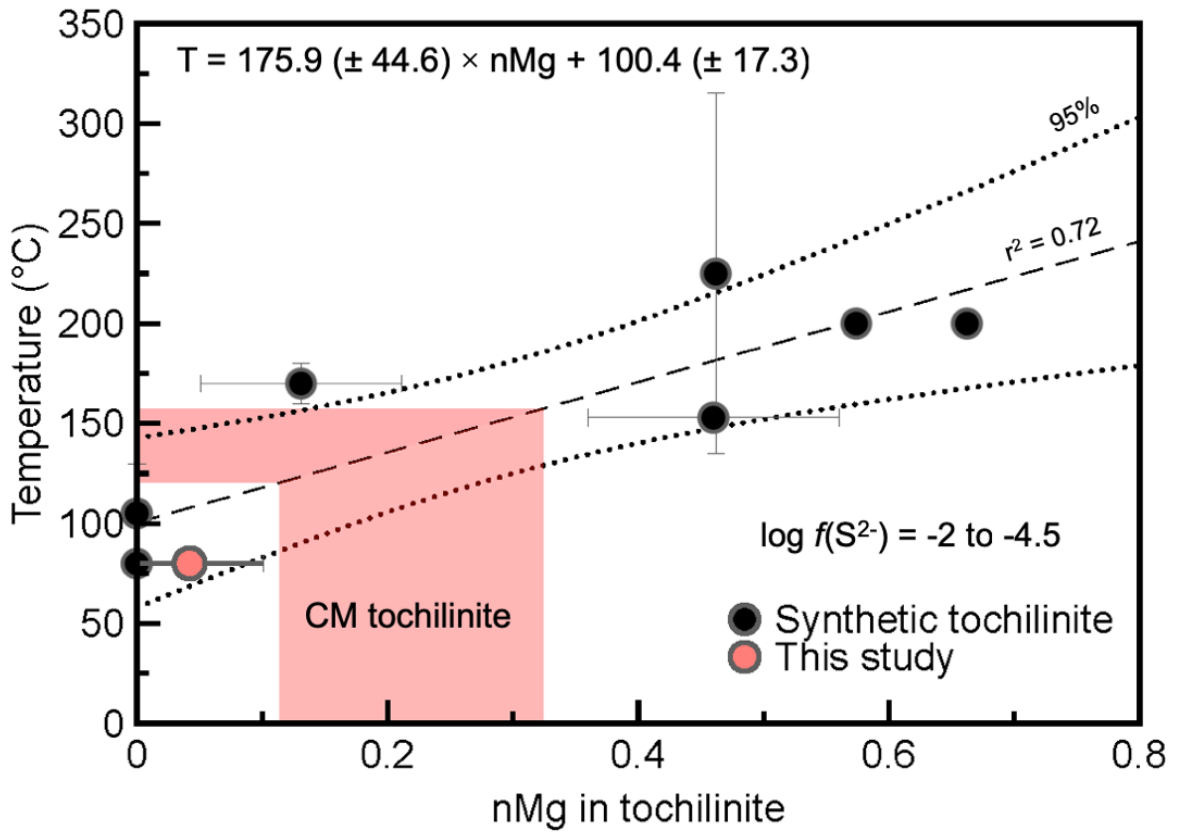


Figure 10

951
 952
 953
 954

955



956
957
958
959

Figure 11

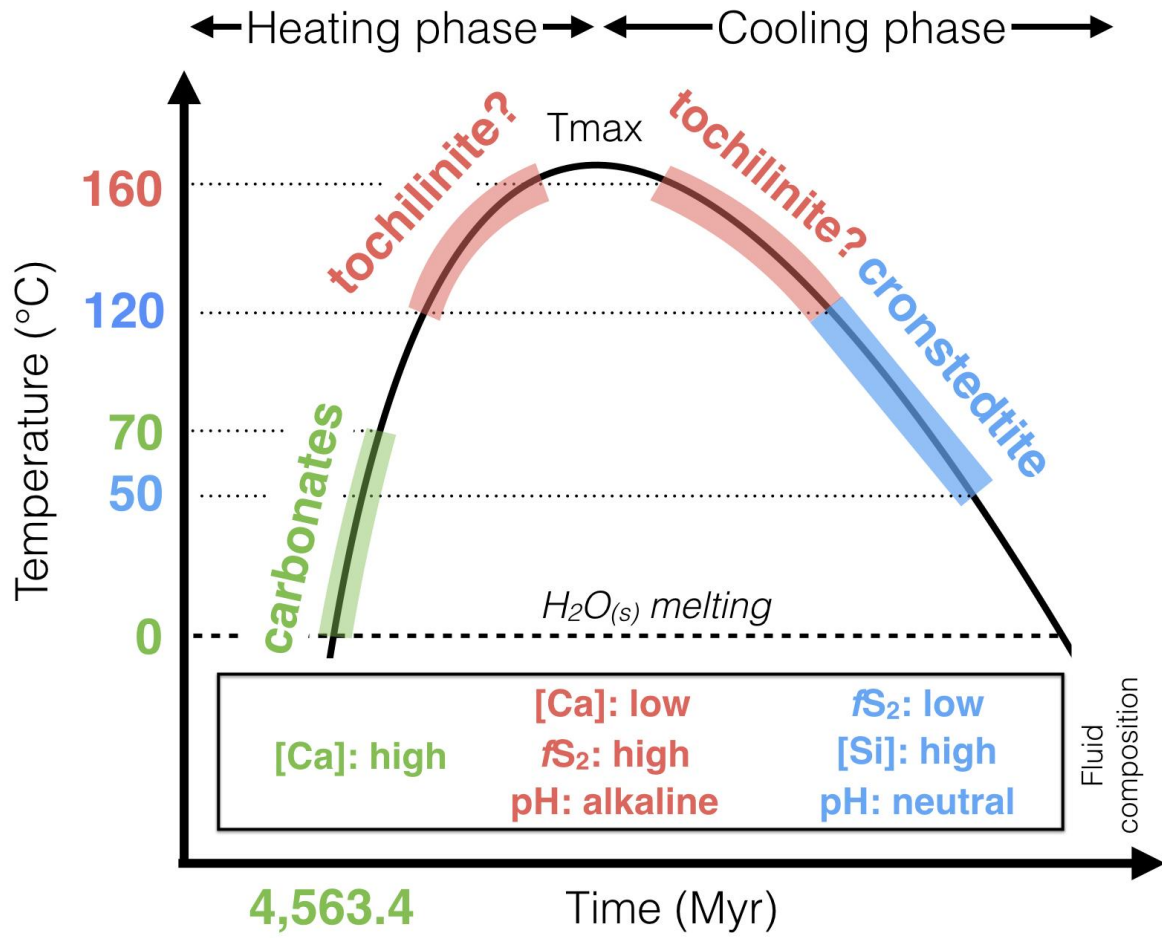
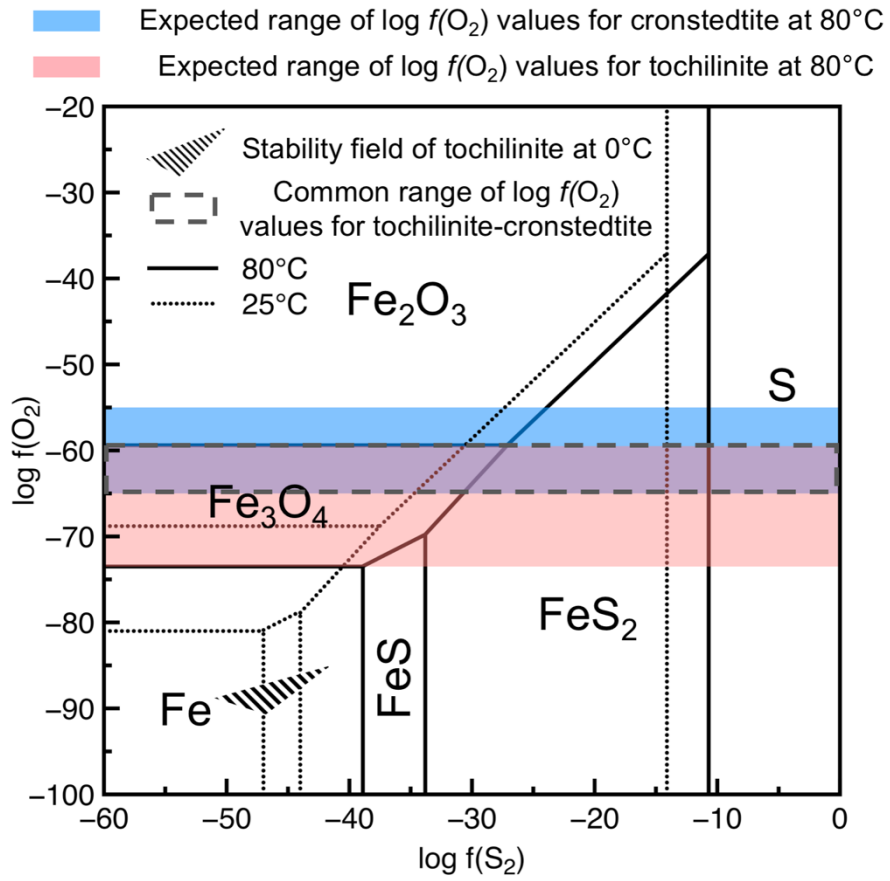


Figure 12

960
 961
 962
 963
 964



965
966

Figure 13

TABLES

Table 1. Summary of anoxic experimental conditions at 80°C and water/rock ratio = 10, and the mineral assemblages synthesized.

Table 2. Summary of hydrothermal syntheses of cronstedtite and (Fe,Mg,Al)-tochilinite.

Table 1

Run #	Synthetic GEMS-like glass (g)	Olivine (g)	Iron metal (g)	Na ₂ S (mM)	Time (d)	Minerals synthesized*
<i>S-free circumneutral fluid (starting pH = 6.5 at 25°C)</i>						
G-1	1	0	< 0.01	0	30	(Fe)-Ph + Go
G-2	1	0	< 0.01	0	60	
GO-1	0.5	0.5	< 0.01	0	30	
GO-2	0.5	0.5	< 0.01	0	60	
GOI-1	0.33	0.33	0.34	0	30	Cr + Go + (Fe)-Ph
GOI-2	0.33	0.33	0.34	0	60	
<i>S-bearing alkaline fluid (starting pH = 11.5 at 25°C)</i>						
GS-1	1	0	< 0.01	10	30	(Fe)-To + (Fe)-Ph + Ox
GS-2	1	0	< 0.01	10	60	
GOS-1	0.5	0.5	< 0.01	10	30	
GOS-2	0.5	0.5	< 0.01	10	60	
GOIS-1	0.33	0.33	0.34	10	30	
GOIS-2	0.33	0.33	0.34	10	60	

* (Fe)-Ph: Fe,Si-rich phyllosilicate; Mt: magnetite; Cr: cronstedtite; (Fe)-To: Fe-rich tochilinite; Go: goethite; Ox: iron oxide.

Table 2

Mineral	Time (days)	Temp. (°C)	pH	Starting material	Authors
Cronstedtite	5-120 45	80	Neutral-alkaline	Smectite + iron metal	Lantenois et al. 2005 Lanson et al. 2012
Cronstedtite	180-365	40-90	Neutral	Claystone + iron metal	Pignatelli et al. 2013, 2014
“Meteoritic” cronstedtite	20-110	110-160	Alkaline	(Fe, Mg, Al)-metal particle precursor mixture	Peng and Jing 2014
Tochilinite	2	200	Neutral-alkaline	(Mg,Al)-hydroxide gel + iron chloride (II)	Kakos et al. 1993
Fe-Tochilinite	10-150	80	Neutral-alkaline	Iron chloride (II)	Kozerenko et al. 1996
Fe-Tochilinite Mg-Tochilinite	30-150	80-360	Alkaline	Iron chloride (II)	Kozerenko et al. 2001
Tochilinite	?	160-180	Medium-alkaline	Same as Kozerenko et al. 1996	Chistyakova et al. 2006 Gubaidulina et al. 2007
(Fe, Mg)-Tochilinite	10-45	120-140	Alkaline	Fe(OH) ₂ + metallic Mg	Moroz et al. 1997
(Fe, Mg, Al)-Tochilinite	4-60 20-110	50-120 110-160	Alkaline	(Fe, Mg, Al)-metal particle precursor mixture	Peng et al. 2007 Peng and Jing 2014
Cronstedtite Fe-Tochilinite	30-60	80	Neutral Alkaline	Glass + olivine + iron metal	This study

979
980

SUPPORTING INFORMATION

981
982
983
984
985
986
987
988
989
990
991
992
993
994
995
996
997
998
999
1000
1001
1002
1003
1004
1005

Fig. S1. BSE images of olivine grains and synthetic GEMS-like grains before and after hydrothermal experiments. a) Pristine olivine and b) synthetic GEMS-like grains before hydrothermal experiments. c) Expected unaltered olivine and d) synthetic GEMS-like grains at micrometer scale in S-free experiments after 60 days of alteration. e) Expected unaltered olivine and f) synthetic GEMS-like grains at micrometer scale in S-rich experiments after 60 days of alteration.

Table S1. Representative chemical compositions of secondary minerals formed during neutral S-free experiments (normalized to 100%); ‘-’ indicates analyses below the detection limit.

Table S2. Dissolved cation concentrations in the run solutions equilibrated with the different synthesized products at 80°C (‘-’ indicates analyses below the detection limit, i.e., <50 µg/L).

Table S3. Representative chemical compositions of secondary minerals formed during alkaline S-rich experiments (normalized to 100%); ‘-’ indicates analyses below the detection limit.

Table S4. Sulfur and Mg concentrations, Mg content in the brucite/amakinite-like layer normalized to 1 S (nMg), and precipitation temperature of synthetic and meteoritic tochilinite. Parenthetical values represent standard deviation; ‘n.d.’ indicates not determined.; ‘n’ indicates the number of values used to calculate the mean nMg value of CM tochilinites. Temperature uncertainties were calculated using the error propagation law.

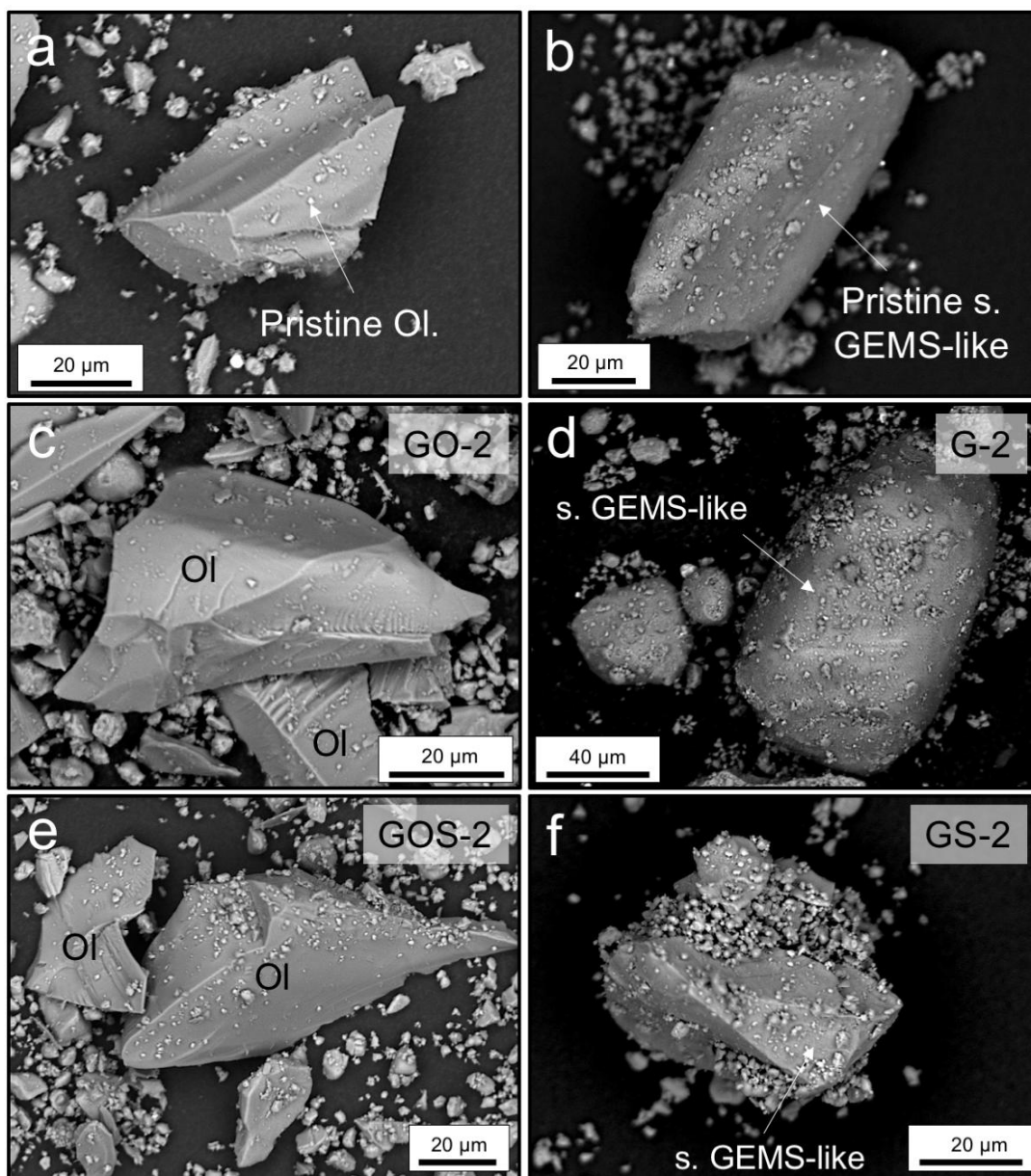


Figure S1

1006
1007
1008

1009

Table S1.

Mineral phase		Si (wt.%)	Mg (wt.%)	Fe (wt.%)	Ca (wt.%)	Al (wt.%)	O (wt.%)	Total
Iron oxide	*	3.6	-	62.3	0.3	-	33.6	100
(Goethite?)	*	2.7	-	67.5	-	-	29.8	100
	*	2.7	-	68.6	-	-	28.8	100
	*	3.0	-	64.2	-	-	32.8	100
	*	3.6	-	64.3	-	-	32.0	100
	*	3.3	-	66.8	-	-	29.8	100
	*	2.9	-	66.6	-	-	30.5	100
	*	2.9	-	66.2	-	-	30.9	100
	*	4.5	1.1	62.4	-	-	32.1	100
	*	3.1	-	66.4	-	-	30.5	100
	*	3.5	-	64.4	-	-	31.7	100
Mean		3.2	0.1	65.4	0.03	-	31.1	
<i>StDev</i>		<i>0.5</i>	<i>0.3</i>	<i>2.0</i>	<i>0.1</i>	<i>-</i>	<i>1.5</i>	
Fibrous Fe,Si-rich	&	18.1	3.7	30.9	0.9	6.3	40.1	100
	&	15.6	1.9	36.9	1.6	3.9	40.2	100
Mean		16.9	2.8	33.9	1.3	5.1	40.2	
<i>StDev</i>		<i>1.8</i>	<i>1.3</i>	<i>4.2</i>	<i>0.5</i>	<i>1.7</i>	<i>0.1</i>	
Cronstedtite	&	8.6	0.6	53.3	0.2	1.7	35.5	100
	&	8.6	0.5	49.6	0.2	1.5	39.6	100
	&	7.9	0.4	55.5	0.1	1.4	34.7	100
	&	8.6	0.4	52.2	0.1	1.2	37.4	100
	&	7.7	0.4	53.7	0.1	1.3	36.9	100
	&	8.5	0.3	52.6	0.2	1.1	37.4	100
Mean		8.3	0.4	52.8	0.2	1.4	36.9	
<i>StDev</i>		<i>0.4</i>	<i>0.1</i>	<i>1.9</i>	<i>0.1</i>	<i>0.2</i>	<i>1.7</i>	

1010

*Data from SEM-EDS analyses.

1011

&Data from TEM-EDS analyses.

1012

1013

Table S2.

Run #	Si (mM)	Mg (mM)	Fe (mM)	Ca (mM)	Al (mM)	Final pH (25 °C)
<i>S-free, circumneutral fluid (starting pH = 6.5 at 25°C)</i>						
G-1	0.93	0.22	43.27	0.36	0.09	6.2
G-2*	0.81	0.04	10 ⁻⁴	0.31	4 x 10 ⁻⁴	6.1
GO-1	1.22	0.44	77.89	0.31	0.13	6.1
GO-2*	0.62	0.03	7 x 10 ⁻⁴	0.30	1.6 x 10 ⁻³	7.9
GOI-1	0.40	0.28	23.10	0.22	0.04	7.2
GOI-2*	0.42	0.04	6 x 10 ⁻⁴	0.24	1.5 x 10 ⁻³	7.8
<i>S-bearing, alkaline fluid (starting pH = 11.5 at 25°C)</i>						
GS-1	2.00	-	-	0.07	0.01	9.8
GS-2	1.66	-	-	0.22	-	7.7
GOS-1	2.02	-	-	0.13	-	10.8
GOS-2	1.94	-	-	0.15	-	8.8
GOIS-1	1.06	0.19	-	0.38	-	6.4
GOIS-2	0.26	-	-	0.10	0.05	9.7

1014

1015

1016

1017

* Because Al, Fe, and Mg concentrations are <50 µg/L, additional aliquots of solution were measured by ICP-MS with a detection limit of 1 µg/L.

1018

Table S3.

Mineral phase		Si (wt.%)	Mg (wt.%)	Fe (wt.%)	Ca (wt.%)	Al (wt.%)	O (wt.%)	S (wt.%)	Total
Fe-rich layer	*	6.6	0.0	53.3	0.5	0.4	34.0	5.2	100
	*	7.3	0.0	47.9	0.7	0.3	36.9	7.1	100
	*	7.8	0.0	43.6	1.3	0.4	39.7	7.2	100
	*	7.1	0.0	54.9	1.4	0.4	29.9	6.4	100
	*	10.3	1.0	42.1	2.4	0.9	37.5	5.7	100
	*	7.4	0.0	47.3	0.9	0.3	35.7	8.5	100
Mean		7.7	0.2	48.2	1.2	0.5	35.6	6.7	
<i>StDev</i>		<i>1.3</i>	<i>0.4</i>	<i>5.1</i>	<i>0.7</i>	<i>0.2</i>	<i>3.4</i>	<i>1.2</i>	
Fe, Si-rich layer	*	24.2	3.6	32.6	2.2	1.9	34.4	1.2	100
Mean		23.3	2.7	33.4	2.0	1.8	36.2	0.6	
<i>StDev</i>		<i>1.2</i>	<i>1.2</i>	<i>1.2</i>	<i>0.2</i>	<i>0.1</i>	<i>2.5</i>	<i>0.9</i>	
Tochilinite	*	6.5	2.1	46.5	1.2	0.9	25.4	17.4	100
	*	5.8	0.8	49.5	1.0	0.8	21.2	20.9	100
	*	4.6	0.4	52.9	1.9	0.4	23.4	16.6	100
	&	2.8	0.1	64.4	0.0	0.4	15.2	17.2	100
	&	2.5	0.0	66.9	0.0	0.6	12.6	17.3	100
	&	1.4	0.3	67.5	0.0	0.3	12.4	18.1	100
Mean		3.9	0.6	57.9	0.7	0.6	18.4	17.9	
<i>StDev</i>		<i>2.0</i>	<i>0.8</i>	<i>9.4</i>	<i>0.8</i>	<i>0.2</i>	<i>5.7</i>	<i>1.5</i>	

1019 *Data from SEM-EDS analyses.

1020 &Data from TEM-EDS analyses.

1021

Table S4.

Meteorite	S (wt.%)	Mg (wt.%)	nMg	Temperature (°C)	Authors
<i>Synthetic tochilinite</i>					
	17.9 (1.5)	0.6 (0.8)	0.04 (0.06)	80	This study
	n.d.	n.d.	0	80	Kozerenko et al. 1996
	n.d.	n.d.	0	80-130	Kozerenko et al. 2001
	15.1 (7.3)	7.1 (3.8)	0.46 (0.1)	153	Peng and Jing 2014
	n.d.	n.d.	0.13 (0.08)	160-170	Chistyakova et al. 2006
	n.d.	n.d.	0.57	200	Kakos et al. 1994
	n.d.	n.d.	0.66	200	Kakos et al. 1994
	n.d.	n.d.	0.46	130-320	Kozerenko et al. 2001
<i>Meteoritic tochilinite (calculated temperatures)</i>					
Paris	18.8 (0.1)	1.6 (0.1)	0.12 (0.004)	122 ± 38	Pignatelli et al. 2017 (n = 2)
Murchison	19 (1.7)	2.6 (0.2)	0.18 (0.02)	132 ± 43	Palmer and Lauretta 2011 (n = 3)
Murray	19.7 (2.9)	2.4 (0.3)	0.17 (0.04)	130 ± 50	Palmer and Lauretta 2011 (n = 3)
Cold Bokkeveld	19.5 (0.7)	4.5 (0.2)	0.32 (0.004)	157 ± 48	Palmer and Lauretta 2011 (n = 1)
Nogoya	18	4.2	0.3	153 ± 47	Palmer and Lauretta 2011 (n = 1)